Bachelor Thesis

Magnetic Shielding

of Space-Based Instruments

Eric Nanowsky

Würzburg, 2023

Julius-Maximilians-Universität Würzburg
Faculty of Physics and Astronomy

Supervisor: Dr. Thomas Siegert

Abstract

Context Cosmic rays that are interacting with the spacecrafts which mount gamma-ray telescopes will result in irreducible instrumental background radiation. Typically, such instruments will have an anti-coincidence shield (ACS) to trigger a veto signal that discards photon measurements in that specific time interval. The issue with the ACS is the enormous mass on the satellite that could be used to increase the detector size. Therefore the idea is to replace the ACS with an electromagnetic shielding method with much less mass.

Aims We want to study the effect of a magnetic shield to deflect charged particles or otherwise shield our detector from cosmic rays in order to avoid the need for a massive ACS. Gamma-ray telescopes could get rid of the AntiCoincidence Shield to make the satellite lighter and possibly increase the size of the detecting system to increase its effective area and be more sensitive to sources in the gamma-ray sky.

Methods We use the propagation of charged particles in a magnetic dipole field that surrounds a cube-shaped detector in order to estimate the efficiency of such a magnetic shield. Here the Forward-Euler, the Explicit Midpoint, and the Runge-Kutta-4-Methods will be applied to solve the differential equations of the Lorentz force numerically.

Results and conclusion The results of the simulations show that the effectiveness of the magnetic shielding process with a 10 T magnetic dipole field is not sufficient to replace the ACS entirely. Other configurations or even higher field strengths have to be considered to achieve the desired results of minimizing the impact rate of cosmic rays onto the telescope.

Zusammenfassung

Kontext Kosmische Strahlung die mit dem Weltraumfahrzeug interagiert, welches Gammastrahlenteleskope transportiert, wird nicht reduzierbaren, instrumentellen Strahlungshintergrund verursachen. Typischerweise sind diese Instrumente mit einem Anticoincidence-Schild (ACS) ausgestattet , das ein Veto-Signal auslöst, um eintreffende Photonenmessungen für einen bestimmten Zeitraum zu verwerfen. Das große Problem ist die enorme Masse des ACS, die auf dem Satelliten angebracht werden muss. Diese Einsparung könnte dafür verwendet werden um den Detektor des Instruments zu vergrößern. Aus diesem Grund ist die Idee das ACS mit einer elektromagnetischen Schildmethode, mit viel geringerer Masse, zu ersetzen.
Ziele Wir möchten die Effekte von einem magnetischen Schild auf geladene Teilchen untersuchen, um diese entweder abzulenken oder anderweitig abzuschirmen, um das massereiche ACS vermeiden zu können. Gammastrahlenteleskope könnten das ACS weglassen um möglicherweise die effektive Detektorfläche zu erhöhen, um sensitiver für Gammastrahlenquellen zu sein.
Methoden Wir benutzen die Propagation von geladenen Teilchen in einem magnetischen Dipolfeld um den kubischen Detektor um die Effizienz von diesem magnetischen Schild zu schätzen. Hierfür werden die numerischen Methoden Forward-Euler, Explicit Midpoint und Runge-Kutta-4 auf die Differentialgleichung der Lorentzkraft angewendet.
Resultate und Schlussfolgerung Die Resultate der Simulationen zeigen das die Effizienz der magnetischen Schildmethode mit einem 10 T magnetischen Dipolfeld nicht genügt um das ACS komplett zu ersetzen. Andere Konfigurationen oder noch stärkere Magnetfelder müssen in Betracht gezogen werden um die gewünschten Resultate von einer verringerten Kollisionsrate der kosmischen Strahlen auf das Teleskop zu realisieren.

Contents

1 Introduction

Humanity's gaze was always directed towards the stars and what lies beyond earth. To collect data from celestial objects we have to observe the electromagnetic radiation coming from all regions of the observable universe. In the photon energy range above 100 keV, called gamma radiation (γ-rays), Earth's atmosphere is absorbing energetic radiation and therefore the telescopes and detectors have to be placed above Earth's atmosphere. Sending instruments into orbit is restricted by the rockets transport capacity of additional objects which limits the possible size of the detector. Limiting factor for gamma-ray observations is that gamma-ray telescopes can hardly focus gamma-rays. Avoiding radiation in the form of photons and cosmic rays from other directions than zenith is crucial. Currently the most effective way to achieve this is with an ACS that is typically much larger and therefore much more massive than the main detector system, thus the detector shrinks compared to the shield, thereby reducing the sensitivity of the instrument. The drawback of the ACS is when a particle interacts with the shield a veto signal is triggered, which increases the dead-time of the detectors. In addition to that the shield is a source of secondary photons when particles interact with the shield to create bremsstrahlung and nuclear excitations. Main contributors of background radiation for our case are primary extragalactic cosmic rays like protons, electrons, positrons and alpha particles [Cumani et al.(2019)]. Terrestrial sources are the Earth's atmosphere owing cosmic-ray interactions as well, and the South Atlantic Anomaly which holds an increased particle density. Additional mechanisms like electron-positron-annihilation, inverse Compton scattering, bremsstrahlung, nuclear excitations, spallation, radioactive build-up and decay and secondary particle production which can undergo all previous interactions are measured continuously depending on the energy range [Siegert et al.(2022)]. Typical source intensities of $10^{-5}\,\mathrm{ph\,cm^{-2}\,s^{-1}}$ would yield a source count of 2500 in a 10^6 second observation window within a total of $3 \cdot 10^7$ SPI event counts [Diehl et al.(2018)]. In this thesis, we investigate a different approach to avoid the need for a massive anti-coincidence shield: By avoiding the ACS of INTEGRAL/SPI, a background rate of 70000-170000 counts per second would impact the measurements. As many of these triggered background events are originating from charged particles, a magnetic shield could potentially replace the need for an ACS altogether. As a first study for soft-gamma-ray telescopes, we are calculating the trajectories of low-energy cosmic rays impinging on a cube-shaped detector as a function of energy and direction. Using this approach, we can scale the problem and open it up for further investigations using particle-by-particle simulations in a full physics setting.

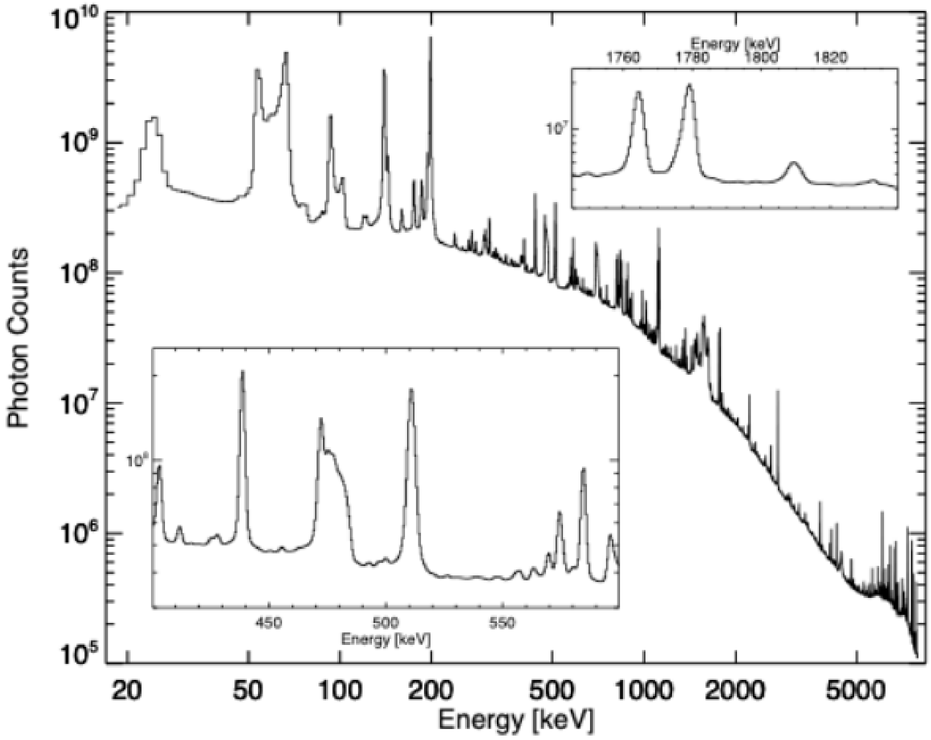

Figure 1.1: Measured (background) energy spectra from SPI during the INTEGRAL mission (orbits 42-1730) [Diehl et al.(2018)].

Figure 1.1 shows the Mission-integrated all-detector spectrum for the orbits 43-1730, while the lower left insert the 511 keV line from positron annihilation and the upper right the 1809 keV ^{26}Al line from diffuse nucleosynthesis indicates. The SPI data consists of events that triggered the Germanium detectors, while the registration of SPI events is disabled by the anticoincidence system triggered by cosmic ray interactions [Diehl et al.(2018)]. We show the background spectrum of primary as well as secondary cosmic rays including atmospheric neutrons in Figure 1.2. While the Flux is dominated by atmospheric neutrons up to the MeV range, cosmic rays dominate the background spectrum throughout the MeV and GeV ranges. In the MeV range the flux from secondary protons, electrons and positrons in a low-Earth orbit (LEO), caused by cosmic ray interactions with Earth's atmosphere, have to be accounted for gamma-ray missions [Cumani et al.(2019)].

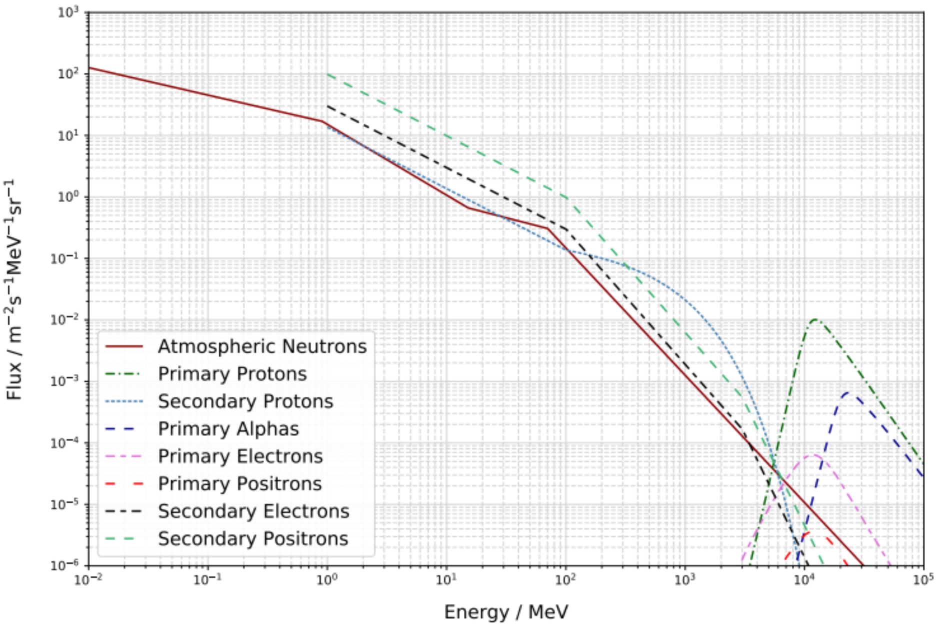

Figure 1.2: Background spectrum for charged cosmic rays and neutrons [Cumani et al.(2019)].

This thesis is structured as follows: In chapter 1, the general outline of the thesis is presented with a short introduction of the established procedure of bringing gamma-ray telescopes into orbit around the earth and the resulting challenges of background radiation from cosmic rays on the instruments. Chapter 2 shows the inspiration of a magnetic shielding method on a gamma-ray telescope from a superconducting toroidal shielding method for manned space exploration. The theoretical foundations for this thesis can be found in Chapter 3, were we explain the Lorentz force and the possible effects magnetic fields have on charged particles. We introduce the numerical methods for the particle trajectory simulations in Chapter 4. The results of the thesis are presented in Chapter 5. We conclude the thesis with a conclusion and an outlook for further exploration of the magnetic shielding concept in Chapter 6.

2 Motivation

The idea for replacing the state-of-the-art shielding method for gamma-ray telescopes is similar to the prospects for magnetic shields via superconducting magnets have been proposed for human spaceflight and in particular long-distance travels, such as to Mars. However, the scale of the magnetic shield surrounding a gamma-ray telescope might be much smaller than for an entire space habitat. To shield humans from dangerous ionizing radiation, from Solar Particle Events and Galactic Cosmic Rays, the concept was to surround the habitable module of the spacecraft with a toroidally shaped superconducting magnet that deflects and/or captures the incoming charged particles. In the same way, the superconducting magnetic shield protects the habitable module we want to see how good a magnetic shield works for any type of soft gamma-ray telescope in orbit with a magnetic field that can be established easily and is considerably lighter than a collimating ACS made of BGO (Bismuth Germanate, $Bi_{12}Ge_3O_{12}$), for example. To visualize this concept, figure 2.1 shows the front and side view of a superconducting, toroidally shaped magnetic system that surrounds the habitable module of the spacecraft. The cosmic rays are supposed to be deflected from any incoming angle to minimize radiation damage for humans.

Active shielding in form of an ACS detects and protects the detectors from photons and charged particles outside the field of view with a typical background count rate of $10^5\,\mathrm{cts\,s^{-1}}$ [Siegert et al.(2022)]. Once an event is triggered in an ACS the shield sends a veto signal and all measurements are discarded for the extent of the veto signal because they do not belong to the measured source inside the field of view. In addition, the detectors are physically protected from all sides except for the area close to the zenith and electronically protected for events happening to the anticoincidence system, visualized in figure 2.2.

We will discuss the influence of an ACS by the example of the spectrometer SPI aboard the INTEGRAL satellite, shown in figure 2.3. The ACS for INTEGRAL is made of 91 BGO scintillator crystal blocks with a mass of 512 kg [von Kienlin et al.(2003)], that are very good gamma-ray and particle absorbers because of the high atomic number due to the bismuth and the high density. The interaction of highly energetic particles with the ACS can create unstable, radioactive isotopes. The decays are delayed secondary radiation features that are measured in addition to the signals from the sky despite the ACS trigger.

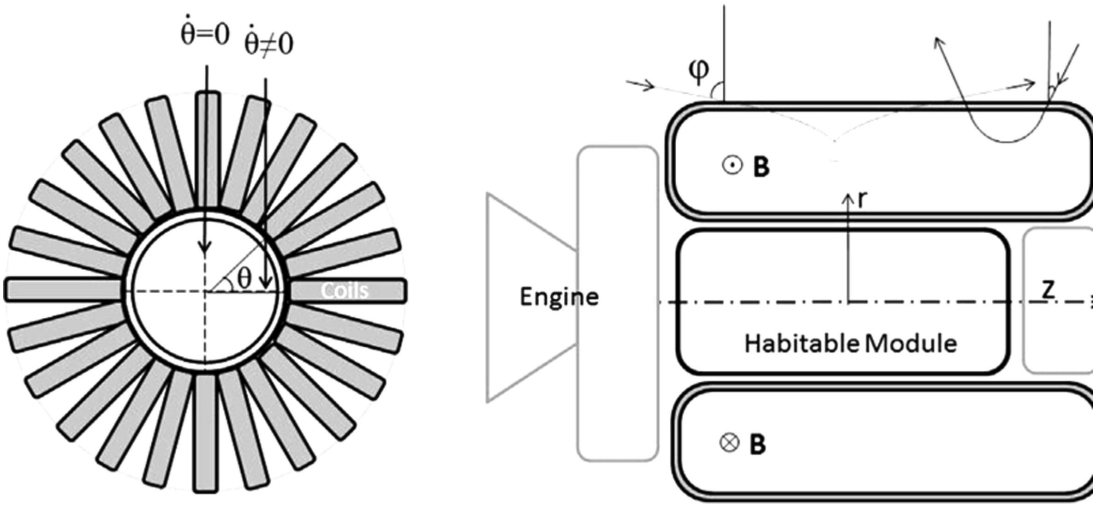

Figure 2.1: This figure shows a schematic diagram of a toroidal space radiation superconducting shield for manned space voyages. Left: Front view with outlined coils. Right: The spacecraft is surrounded by the coils that produce a magnetic field that envelops the habitable module. The pitch angle ϕ indicates the angle between the magnetic field and the momentum vector of the particle and is one factor that dictates the trajectory taken by the cosmic rays [Al Zaman et al.(2021)].

Now instead of letting galactic cosmic rays in the form of (ultra-)relativistic electrons, protons, and helium nuclei interact with the protective shield we want to deflect and/or capture, using magnetic fields, these charged particles so that they are prevented from interacting with the detectors. This would allow for more desired events to be registered and might in addition even avoid radiation damage to the spacecraft and instrument components.

The ACS is large in size and mass that restricts the geometric and effective area of the 19 high purity germanium detectors with the covered area being $500\,cm^2$ [Schanne et al.(2003)]. For effective use the Ge detectors are cooled to 85 K with an active cryogenic system. The spectrometer can therefore provide an energy resolution of 2 keV for 1 MeV photons which is 10 times better than prior telescopes. Below the mask a 5 mm thick plastic scintillator (PSAC) is placed that permits the rejection of events from prompt mask activation [Schanne et al.(2003)]. If we removed the $10000\,\mathrm{cm}^2$ [Siegert et al.(2022)] ACS and replaced it, the magnetic shielding mechanism would have to deflect 70000-170000 counts per second in the case of INTEGRAL/SPI.

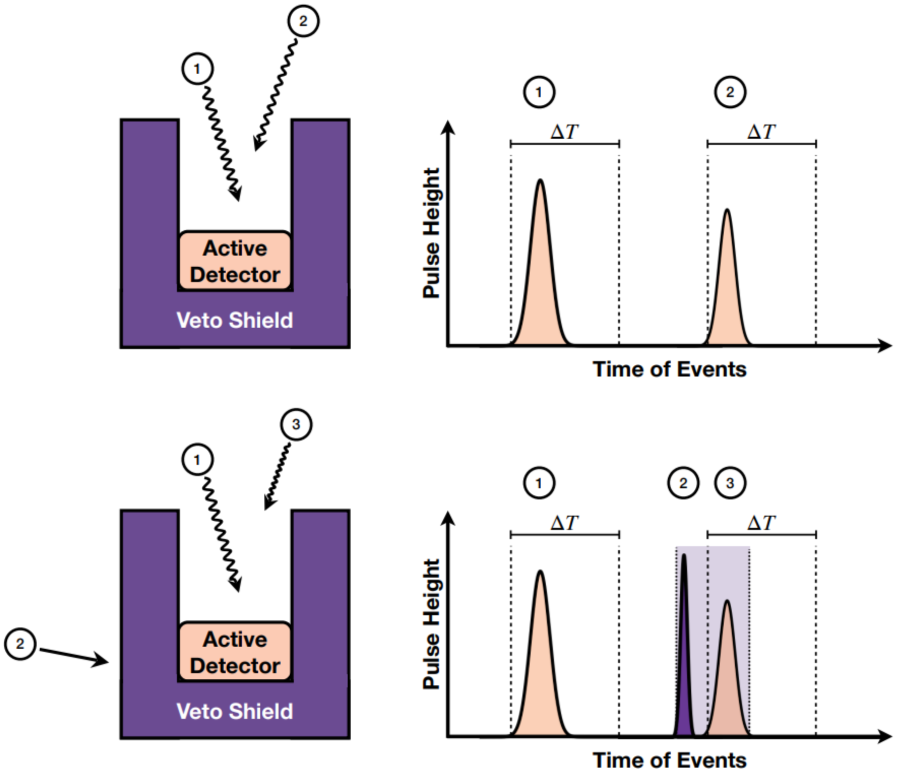

Figure 2.2: The top image shows two incoming photons from within the field of view and deposit their energies in the active detector (left). When a pulse is registered for each event, the detecting system is unable to record new pulses due to the dead time ΔT from the signal (right). The bottom image has an outside particle event that hits the veto shield after the photon event (1) but before the photon event (3). The registered pulse for event (1) stays the same but particle (2) triggers a veto signal (purple range, right) that vetoed both registered events (2) and (3) [Siegert et al.(2022)].

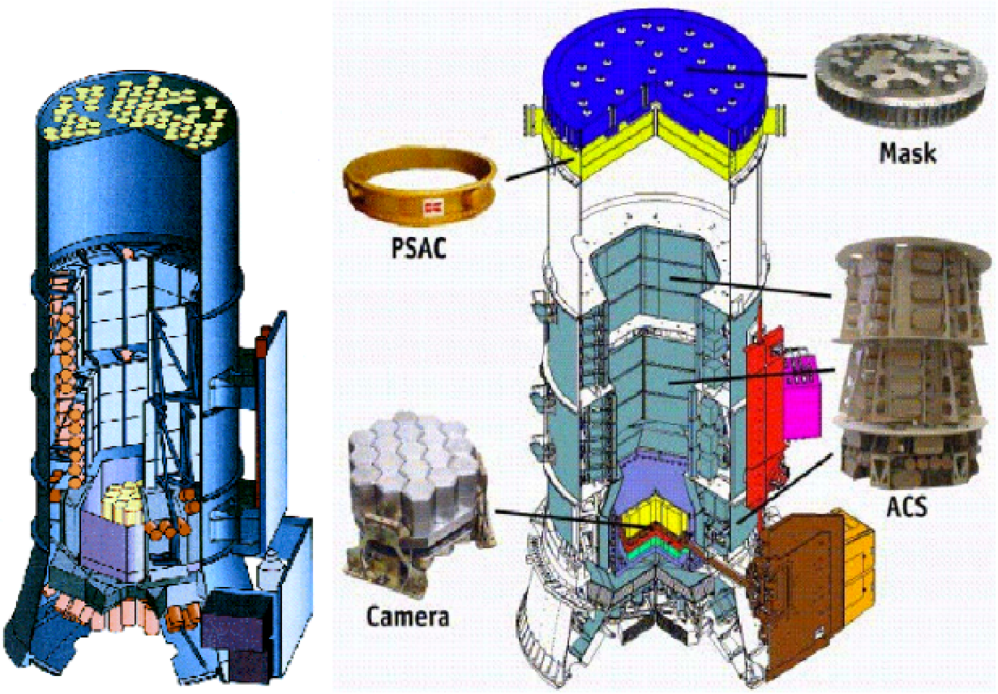

Figure 2.3: SPI instrument on the INTEGRAL satellite with a schematic depiction (left) and the exposed components (right). The crucial elements are the 19 Ge detector camera mounted in a cryostat, a coded mask with tungsten elements blocking parts of the field of view, the anti-coincidence detector system (ACS) surrounding the entire instrument using BGO scintillators and a plastic scintillator plate (PSAC), each with photomultiplier tubes [Diehl et al.(2018)].

3 Theoretical foundation of charged particle motion

3.1 Lorentz force

The most fundamental concept that describes the trajectories of charged particles in electric and magnetic fields is the Lorentz force. The Lorentz force in its general, non-relativistic form is made up of the electric component $\vec{F}_E$ and the magnetic component $\vec{F}_B$.

$$\vec{F} = \vec{F}_E + \vec{F}_B = q \cdot (\vec{E}(\vec{r}(t), t) + \vec{v}(t) \times \vec{B}(\vec{r}(t), t)) = q \cdot (\vec{E}(\vec{r}(t), t) + \dot{\vec{r}}(t) \times \vec{B}(\vec{r}(t), t)) \quad (3.1)$$

The Lorentz force is determined by the charge q, the velocity of the charged particle v(t), the external electric field $\vec{E}(\vec{r}(t), t)$ and the external magnetic field $\vec{B}(\vec{r}(t), t)$. The electric and magnetic fields that satisfy the Lorentz force also have to satisfy Maxwell's equations and are therefore bound by energy- and momentum conservation laws. The mechanical work exerted by a point charge at a position $\vec{r}(t)$ in an electromagnetic field with an infinitesimal displacement $d\vec{s} = \vec{v}dt$ can be expressed by:

$$dW^{mech} = \vec{F} \cdot d\vec{s} = q \cdot (\vec{E}(\vec{r}(t), t) + \vec{v} \times \vec{B}(\vec{r}(t), t)) \cdot \vec{v} \cdot dt = q \cdot \vec{E}(\vec{r}(t), t) \cdot \vec{v}(t) \cdot dt \quad (3.2)$$

Equation (3.2) shows that in dynamic systems the magnetic field does not exert any mechanical work on a point charge. It changes the direction of velocity that is equivalent to acceleration but not the absolute value of the velocity vector. The reason for this is that the forces caused by the magnetic fields are always perpendicular to the current direction of the velocity vector. Compared to this, electric fields cause forces so that the velocity vector follows the electric field lines causing an acceleration that changes the absolute value of the velocity vector because they exert work on charged particles shown in equation (3.2). For systems without an electric field $\vec{E}$, equation (3.2) vanishes and we can conclude energy conservation that leaves the absolute value of the velocity vector unchanged:

$$|\vec{v}| = \text{constant}$$

3.1.1 Non-relativistic Lorentz force

Solving the Lorentz force analytically, in its general form, without an electric field $\vec{E}$, we can turn a second-order differential equation

$$\frac{d^2\vec{r}(t)}{dt^2} = \frac{q}{m} \cdot \left(\frac{d\vec{r}(t)}{dt} \times \vec{B}(\vec{r}(t), t) \right) \tag{3.3}$$

into six linked differential equations of the first order [Bartelmann (2015)]:

$$\dot{v_x}(t) = \frac{q}{m} \cdot ((v_y(t) \cdot B_z) - (v_z(t) \cdot B_y)) \tag{3.4}$$

$$\dot{v_y}(t) = \frac{q}{m} \cdot ((v_z(t) \cdot B_x) - (v_x(t) \cdot B_z)) \tag{3.5}$$

$$\dot{v_z}(t) = \frac{q}{m} \cdot ((v_x(t) \cdot B_y) - (v_y(t) \cdot B_x)) \tag{3.6}$$

$$\dot{x} = v_x(t) \tag{3.7}$$

$$\dot{y} = v_y(t) \tag{3.8}$$

$$\dot{z} = v_z(t) \tag{3.9}$$

with $v_x(t)$, $v_y(t)$ and $v_z(t)$ being the components of the velocity vector $\vec{v}(t)$ and B_x, B_y, and B_z being the components of the magnetic field $\vec{B}(\vec{r}(t), t)$.

3.1.2 Relativistic Lorentz force

The Lorentz force in its non-relativistic form, shown in 3.1.1, can only be used as an approximation for non-relativistic particle velocities $v \ll c$. The fully relativistic form of the Lorentz force that is sufficient to correctly explain trajectories of cosmic rays uses the relativistic expression for the momentum $\mathrm{p} = \gamma\mathrm{mv}$ instead of the classical momentum $p = mv$ with $\gamma^2 = \frac{1}{1-\vec{\beta}^2}$ and and $\vec{\beta} = \frac{\vec{v}(t)}{c}$, so that $\gamma \equiv\gamma(\vec{v}(t))$ being the Lorentz factor [Longair (2014)]:

$$\frac{d}{dt}(\gamma m\dot{\vec{r}}(t)) = q \cdot (\dot{\vec{r}}(t) \times \vec{B}(\vec{r}(t), t)) \tag{3.10}$$

Because the Lorentz-Factor is a function of the velocity vector the time derivative of the factor on the left side of the equation (3.10) in a magnetic field is:

$$\frac{d}{dt}(\gamma m\vec{v}(t)) = \dot{\gamma} m\vec{v}(t) + \gamma m\dot{\vec{v}}(t) = m\left[\left(-\frac{1}{2}\right) \cdot \gamma^3 \cdot \left(-\frac{1}{c^2}\right) \cdot (\vec{v} \cdot \vec{a} + \vec{a} \cdot \vec{v}) + \gamma\vec{a}\right] = \gamma m\vec{a} \tag{3.11}$$

The relativistic form of the Lorentz force is similar to the differential equation (3.3) with an additional factor of $\frac{1}{\gamma}$:

$$\frac{d^2\vec{r}(t)}{dt^2} = \frac{q}{\gamma m} \cdot \left(\frac{d\vec{r}(t)}{dt} \times \vec{B}(\vec{r}(t), t) \right) \tag{3.12}$$

and the six linked differential equations:

$$\dot{v_x}(t) = \frac{q}{\gamma m} \cdot ((v_y(t) \cdot B_z) - (v_z(t) \cdot B_y)) \tag{3.13}$$

$$\dot{v_y}(t) = \frac{q}{\gamma m} \cdot ((v_z(t) \cdot B_x) - (v_x(t) \cdot B_z)) \tag{3.14}$$

$$\dot{v_z}(t) = \frac{q}{\gamma m} \cdot ((v_x(t) \cdot B_y) - (v_y(t) \cdot B_x)) \tag{3.15}$$

$$\dot{x} = v_x(t) \tag{3.16}$$

$$\dot{y} = v_y(t) \tag{3.17}$$

$$\dot{z} = v_z(t) \tag{3.18}$$

3.1.3 Abraham-Lorentz force

In the previous sections for the Lorentz force, we did not take radiation losses due to synchrotron radiation into account. By emitting photons, the charged particle will slow down because of the energy losses. The derivation starts by investigating the energy lost per unit of time using Larmor's formula [Longair (2014)].

$$\int_{t_1}^{t_2} \vec{F}_{\mathrm{AL}} \cdot \vec{v}\, dt = -\int_{t_1}^{t_2} \frac{dE}{dt}\, dt = -\frac{q^2}{6\pi\epsilon_0 c^3} \int_{t_1}^{t_2} \frac{d\vec{v}}{dt} \cdot \frac{d\vec{v}}{dt}\, dt \tag{3.19}$$

The last integral can be solved with integration by parts and applying that the first term $\vec{v} \cdot \vec{a}$ vanishes for circular motion, e.g. in magnetic fields.

$$\int_{t_1}^{t_2} \frac{d\vec{v}}{dt} \cdot \frac{d\vec{v}}{dt}\, dt = \int_{t_1}^{t_2} \dot{\vec{a}} \cdot \vec{v}\, dt$$

$$\int_{t_1}^{t_2} \vec{F}_{\mathrm{AL}} \cdot \vec{v}\, dt = \int_{t_1}^{t_2} \frac{q^2}{6\pi\epsilon_0 c^3} \dot{\vec{a}} \cdot \vec{v}\, dt \tag{3.20}$$

Now by comparing both integrals, we found an expression for the radiation reaction force, also known as the Abraham-Lorentz force, that has a dependence on the time-derivative of the acceleration of the particle.

$$\vec{F}_{\mathrm{AL}} = \frac{q^2}{6\pi\epsilon_0 c^3} \dot{\vec{a}} \equiv m\tau\dot{\vec{a}} \tag{3.21}$$

with $\tau = \frac{q^2}{6\pi\epsilon_0 c^3 m}$ being the characteristic time scale for the energy loss. With the addition of the radiation reaction force, the Lorentz force takes on the form of a fourth-order differential equation.

$$\frac{d^2\vec{r}(t)}{dt^2} = \frac{q}{m} \cdot \left(\frac{d\vec{r}(t)}{dt} \times \vec{B}(\vec{r}(t), t) \right) - m\tau \frac{d^3\vec{r}(t)}{dt^3} \tag{3.22}$$

By comparing the characteristic timescales of the electron, proton, and alpha particle we can determine if the Abraham-Lorentz force is a non-negligible term that we have to consider when doing our calculations of the particle trajectories.

$$\gamma ma = qvB\sin(\theta) \tag{3.23}$$

$$a = \frac{qB}{\gamma m} v \sin(\theta) \tag{3.24}$$

with θ being the pitch angle. The pitch angle is the angle between the momentum vector of the particle and the magnetic field lines. By averaging over all possible and random pitch angles, we can calculate the expectation value of $\sin(\theta)$ to be:

$$\langle \sin(\theta) \rangle = \frac{1}{4\pi} \int_{-\pi}^{\pi} \sin(\theta)\, d\theta \int_{0}^{2\pi} \sin(\theta)\, d\phi = \frac{1}{4} \tag{3.25}$$

Therefore we can now express the characteristic timescale as $T_g = \gamma \frac{2\pi m}{qB}$ for the Lorentz force and $\tau_{\mathrm{AL}} = \frac{q^2}{6\pi\epsilon_0 c^3 m}$ for the Abraham-Lorentz force. For highly relativistic particles of around $\gamma = 22$ and a magnetic field strength of $B = 1\,\mathrm{T}$ we can calculate:

Electron

$$T_g = 8.00 \cdot 10^{-10}\,\mathrm{s}$$

$$\tau_{\mathrm{AL}} = 6.25 \cdot 10^{-24}\,\mathrm{s}$$

Proton

$$T_g = 1.47 \cdot 10^{-6}\,\mathrm{s}$$

$$\tau_{\mathrm{AL}} = 3.40 \cdot 10^{-27}\,\mathrm{s}$$

Alpha-Particle

$$T_g = 2.92 \cdot 10^{-6}\,\mathrm{s}$$

$$\tau_{\mathrm{AL}} = 3.43 \cdot 10^{-27}\,\mathrm{s}$$

From comparing the characteristic timescales we can conclude that the Abraham-Lorentz force is negligible compared to the Lorentz force for regular magnetic field strengths because it is many orders of magnitude smaller for all the listed particles $\tau_{\mathrm{AL}} \ll T_g$. To compare the strength of the Abraham-Lorentz force and the (relativistic) Lorentz force we can equate the two timescales and solve for the magnitude of the magnetic field.

$$T_g = \tau_{\text{AL}}$$
$$\frac{2\pi\gamma m}{qB} = \frac{q^2}{6\pi\epsilon_0 c^3 m}$$
$$B = \gamma\frac{12\pi^2 m^2\epsilon_0 c^3}{q^3}$$

For the radiation reaction force to be as strong as the Lorentz force for an electron traveling at $v = 0.999c$, the magnetic field has to be of the strength $B = 1.3 \cdot 10^{18}\,\text{G} = 1.3 \cdot 10^{14}\,\text{T}$. These magnetic fields can only be found in highly magnetized rotating neutron stars, called magnetars.

3.2 Effects of magnetic fields on charged particles

3.2.1 Circular motion

The simplest case for a charged particle in a homogenous and constant magnetic field is a magnetic field pointing in a specific direction. The three-dimensional cartesian coordinate system can be chosen so that one of the coordinate axis, here without the loss of generality the z-coordinate, has a parallel alignment to the magnetic field vector $\vec{B} = B \cdot \vec{e}_z$.

$$\dot{v_x}(t) = \frac{qB}{\gamma m} \cdot v_y(t) = \omega_g^2 \cdot v_y(t) \tag{3.26}$$

$$\dot{v_y}(t) = -\frac{qB}{\gamma m} \cdot v_x(t) = -\omega_g^2 \cdot v_x(t) \tag{3.27}$$

$$\dot{v_z}(t) = 0 \tag{3.28}$$

with $\omega_g^2 = \frac{qB}{\gamma m} = \frac{\omega_0^2}{\gamma}$ being the relativistic gyro frequency and in the non-relativistic case the non-relativistic gyro frequency is defined as $\omega_0^2 = \frac{qB}{m}$. Another time derivative lets us decouple the remaining differential equations:

$$\ddot{v_x}(t) = -\omega_g^2 \cdot v_x(t) \tag{3.29}$$

$$\ddot{v_y}(t) = -\omega_g^2 \cdot v_y(t) \tag{3.30}$$

This harmonic oscillator form can be solved with the standard ansatz $v(t) = A \cdot \sin(\omega_g t)$. If we rotate the coordinate system so that one velocity coordinate equals zero, here $v_y(0)$ for $t = 0$, we can express the velocity vector as:

$$\vec{v}(t) = \begin{pmatrix} v_x(0) \cdot \cos(\omega_g t) \\ -v_x(0) \cdot \sin(\omega_g t) \\ v_z(0) \end{pmatrix} \tag{3.31}$$

Through integration with respect to the time t, we can get an analytical expression for the trajectory of the charged particle of:

$$\vec{x}(t) = \vec{x}(0) + \begin{pmatrix} \frac{v_x(0)}{\omega_g} \cdot \sin(\omega_g t) \\ \frac{v_x(0)}{\omega_g} \cdot (cos(\omega_g t) - 1) \\ v_z(0) \cdot t \end{pmatrix} \tag{3.32}$$

If the initial velocity in the z-direction $v_z(0) = 0$ is zero, the charged particle will move in a circular motion inside the magnetic field. In the other case for $v_z(0) \neq 0$ the charged particle will trace the path in form of a helix and that velocity will not change because there is no acceleration vector parallel to the magnetic field.

If the charged particle enters the magnetic field with a certain pitch angle θ it will follow a helix-form trajectory because of the parallel and perpendicular components of the velocity vector.

$$\vec{v} = \vec{v}_{\|} + \vec{v}_{\perp} \tag{3.33}$$

Because only the perpendicular component is relevant for the Lorentz force, the differential equation adapts the form [Longair (2014)]:

$$\gamma m \vec{a} = qvB\sin(\theta) \cdot (\vec{e}_v \times \vec{e}_B) \tag{3.34}$$

with $v_{\perp} = v \cdot sin(\theta)$. Due to the Lorentz force forcing charged particles to gyrate, we can define another important and characteristic quantity called the gyro-radius r_g. To determine r_g we have to equate the magnitude of the Lorentz force with the centripetal force [Longair (2014)].

$$\frac{\gamma m v_{\perp}^2}{r_g} = |q| v_{\perp} B \tag{3.35}$$

$$r_g = \frac{\gamma m v_{\perp}}{|q| B} \tag{3.36}$$

3.2.2 Magnetic mirror effect

The magnetic mirror effect is possible when particles with a magnetic moment experience an increasing force that causes them to reverse direction or be reflected if certain conditions are met. Particles with a magnetic moment in a magnetic field have the potential energy of $V = -\mu B$. Due to the inhomogeneity of a magnetic dipole field, in our case, the potential energy has a resulting force on the magnetic moment. This force acting on the magnetic moment can be expressed as an additional added force to the non-relativistic Lorentz force equation (3.3):

$$\vec{F}_{\text{ext}} = \mu \vec{\boldsymbol{\nabla}} B \tag{3.37}$$

while the magnetic moment is defined as

$$\mu = \frac{mv_\perp^2}{2B} = \frac{E_{kin,\perp}}{B} \tag{3.38}$$

To derive the mirror ratio and the criteria for particle reflection we have to prove the conservation of the magnetic moment in inhomogeneous magnetic fields. This can be achieved by using adiabatic invariants. These variables I are defined by:

$$I = \int p\, dq \tag{3.39}$$

with p and q being the conjugate canonical variables. The classical Hamiltonian for an electric charge e with the corresponding momentum vector $\vec{p}$ in a magnetic field can be written as:

$$H(\vec{p}, \vec{q}) = \frac{1}{2m}(\vec{p} - e\vec{A})^2 \tag{3.40}$$

$$\vec{p} = m\vec{v} + e\vec{A} \tag{3.41}$$

with $\vec{A}$ being the magnetic vector potential describing the magnetic magnetic field $\vec{B} = \vec{\boldsymbol{\nabla}} \times \vec{A}$. The first adiabatic invariant I_1 can therefore be expressed as the integral over one loop of one gyro circle:

$$I_1 = \int m\vec{v}\, d\vec{r} + \int e\vec{A}\, d\vec{r} \tag{3.42}$$

$$= \frac{2\pi m^2 v_\perp^2}{eB} + \frac{\pi m^2 v_\perp^2 eB}{e^2 B^2} = \frac{3\pi m^2 v_\perp^2}{eB} = \frac{6\pi m}{e}\mu \propto \mu \tag{3.43}$$

This result can be interpreted as a conservation of the magnetic moment. Because the magnetic moment is constant and the kinetic energy is constant we can use

$$\frac{1}{2}m \cdot (v_\perp^2 + v_\parallel^2) = \mu B + \frac{1}{2}mv_\parallel^2 \tag{3.44}$$

By using the kinetic energy and the magnetic moment as constants we can conclude that in the regions with increasing magnetic field strength, the perpendicular velocity component will increase while the parallel velocity component will decrease. The particle reflection will occur when $v_\parallel \overset{!}{=} 0$ is met.

$$\frac{1}{2}mv_\parallel^2 + \mu B_\text{min} \leq \mu B_\text{max} \tag{3.45}$$

The mirror ratio describes the boundary condition for the particle, therefore confining the particle to the inhomogeneous magnetic field. By rearranging the terms in equation (3.45) we arrive at:

$$\frac{v_{\parallel,0}}{v_{\perp,0}} \leq \sqrt{\frac{B_\text{max}}{B_\text{min}} - 1} \tag{3.46}$$

Figure 3.1 shows the electron gyrating along the magnetic field lines in three cartesian planes and reflected near the poles due to the magnetic mirror effect.

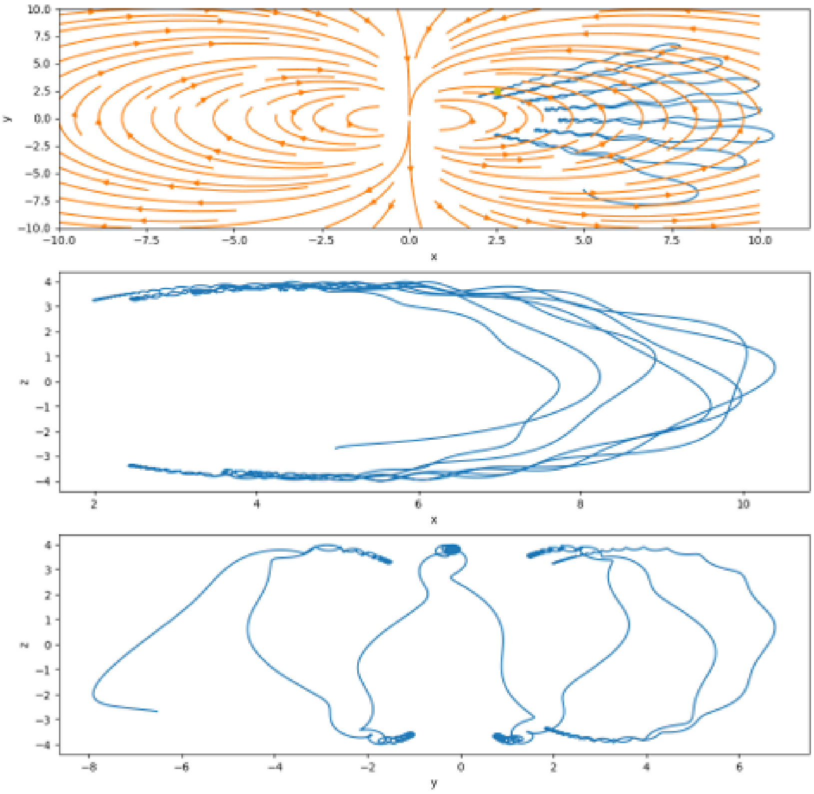

Figure 3.1: The figure shows an electron trajectory with 2 MeV kinetic energy, the incident angle of $\theta = 90^\circ$ and $\phi = 90^\circ$ in a 1 T magnetic dipole field. The electron goes through many bounce periods along the magnetic field lines and always gets reflected due to the magnetic mirror effect near the poles of the dipole field.

3.2.3 Particle capture

Certain configurations can cause the charged particle to be captured in the magnetic field, comparable to Earth's magnetic field. Once they are captured the particles will go through many bounce periods, defined by the time particles move between two mirror points and the azimuthal magnetic drift.

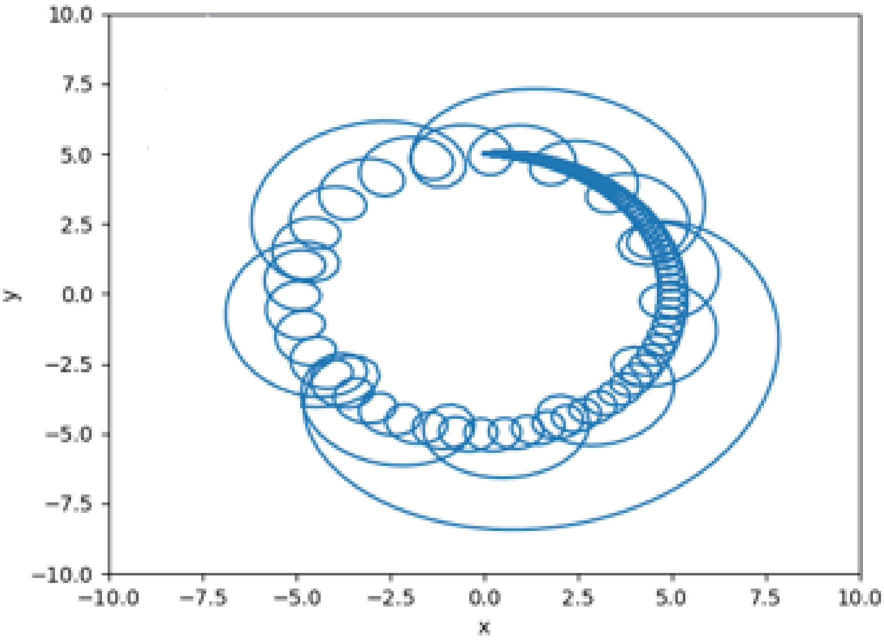

Figure 3.2: The figure shows an electron trajectory with 2 MeV kinetic energy, the incident angle of $\theta = 45\,^{\circ}$ and $\phi = 45\,^{\circ}$ in a 1 T magnetic dipole field that was captured and is gyrating circularly around the origin.

4 Numerical Particle Simulations

For the simulation of a charged particle's trajectory, we need to resort to numerical methods, because the magnetic fields used do not give an analytical solution to the six differential equations (3.13) - (3.18). These approximation algorithms allow us to decide how precise the calculations are supposed to be which ultimately depends on the chosen time steps. As a result of solving the differential equations numerically we get particle trajectories with numerical values for each time step evaluated at that iteration step.

4.1 Numerical methods

In this section, a few common approximation algorithms will be explained, and how they are implemented in the Python program for solving the differential equations numerically.

4.1.1 Forward Euler

The Forward Euler method is the simplest explicit first-order method for solving differential equations numerically, given an initial value. The process of estimating the original curve of the solution starts with the initial value $y(t_0) = y_0$ for a given starting time t_0. The Euler method is given by equation (4.1) that allows us to calculate the next value given the previously calculated value

$$\mathrm{y_{n+1}} = \mathrm{y_n} + \mathrm{h} \cdot f(\mathrm{t_n}, \mathrm{y_n}) \tag{4.1}$$

with $h = \mathrm{t_{n+1}} - \mathrm{t_n}$ being the constant step size defined by the next point in time $\mathrm{t_{n+1}}$ and the current time point $\mathrm{t_n}$ [Münster (2016)]. Ordinary differential equations of the form $\dot{y} = f(\mathrm{t_n}, \mathrm{y_n})$ give us the slope of the function in form of a tangent line at a specific point. The slope of the tangent line, in combination with the step size and the initial value of the iteration step, is used to calculate the next point. To increase the precision of this numerical method is to shorten the step size of the computation.

4.1.2 Explicit Midpoint

The Explicit Midpoint Method distinguishes itself from the other methods by evaluating the slope at the middle of the two time points $\mathrm{t_n}$ and $\mathrm{t_{n+1}}$ by replacing $\mathrm{t_n}$ with $\mathrm{t_{n+1/2}} =$

$\mathrm{t_n} + \frac{\mathrm{h}}{2}$ [Münster (2016)].

$$\mathrm{y_{n+1}} = \mathrm{y_n} + \mathrm{h} \cdot f(\mathrm{t_n} + \frac{h}{2}, \mathrm{y_n} + \frac{h}{2} \cdot f(\mathrm{t_n}, \mathrm{y_n})) \tag{4.2}$$

4.1.3 Runge-Kutta

The more accurate method is the Runge-Kutta-4-Method because it takes into account four slopes coming from k_1 to k_4 and averaging out between them. This approximation technique calculates the next timestep-value $\mathrm{y_{n+1}}$ by using the current value $\mathrm{t_n}$ and adding weighted terms of previous numerical methods.

$$k_1 = f(\mathrm{t_n}, \mathrm{y_n}) \tag{4.3}$$

$$k_2 = f(\mathrm{t_n} + \frac{h}{2}, \mathrm{y_n} + \frac{h}{2} \cdot k_1) \tag{4.4}$$

$$k_3 = f(\mathrm{t_n} + \frac{h}{2}, \mathrm{y_n} + \frac{h}{2} \cdot k_2) \tag{4.5}$$

$$k_4 = f(\mathrm{t_n} + h, \mathrm{y_n} + h \cdot k_3) \tag{4.6}$$

Listing the needed values k_1 to k_4 we can identify k_1 to be the slope at the starting value for every timestep using $\mathrm{y_n}$, comparable to Euler's Method. The values of k_2 and k_3 are the expression for the slope in the middle of the computation interval for $\mathrm{y_n}$ and k_1 as well as $\mathrm{y_n}$ and k_2, respectively (Explicit Midpoint Method). The interpretation of k_4 is the slope at the calculated point $\mathrm{y_{n+1}}$ using the initial value $\mathrm{y_n}$ and k_3. In the final equation, the values k_2 and k_3 are weighted more than k_1 and k_4, giving us [Münster (2016)]:

$$\mathrm{y_{n+1}} = \mathrm{y_n} + \frac{h}{6} \cdot (k_1 + 2k_2 + 2k_3 + k_4) \tag{4.7}$$

4.2 Particle Trajectories

Due to the relativistic nature of our problem, we have to express the starting velocity as a function of the kinetic energy of the particle. To derive a suitable expression we have to start with the fully relativistic form of the total energy E with the familiar forms of $E = E_{\mathrm{Kin}} + E_0$ and $p = \gamma m_0 v$:

$$\begin{gathered} E^2 = p^2c^2 + m_0^2c^4 = \gamma^2 m_0^2 v^2 c^2 + m_0^2 c^4 \qquad (4.8) \\ E^2\left(1 - \frac{m_0^2c^4}{E^2}\right) = \gamma^2 m_0^2 v^2 c^2 \\ \left(1 - \frac{m_0^2c^4}{E^2}\right) = \frac{v^2}{c^2} \end{gathered}$$

$$\Rightarrow \frac{v}{c} = \sqrt{\left(1 - \left(\frac{m_0c^2}{E_{\text{Kin}} + m_0c^2}\right)^2\right)}$$

For a more specific starting point of the cosmic rays used in the differential equations, we can do a coordinate transformation from cartesian coordinates to spherical coordinates depending on the given magnetic field and the symmetries of the situation. In this case, the coordinate transformation transforms the three spatial coordinates (x, y, z) to the corresponding spherical coordinates (r, θ, φ) with r being the radial distance from the origin to the location of the charged particle, θ the polar angle with respect to the polar axis (z-axis) and φ the azimuthal angle with respect to the x-axis in the initial x-y-plane. The background spectrum of charged particles [Cumani et. al, 2019] for the three considered particles was obtained at an equatorial orbit of 550 km.

The primary magnetic field used for modeling the magnetic shielding process is the magnetic dipole field. In spherical coordinates, the magnetic dipole takes on the form of:

$$B(\vec{r}) = \frac{\mu_0}{4\pi r^2}\frac{3\vec{r}(\vec{m}\cdot\vec{r}) - \vec{m}r^2}{r^3} \tag{4.9}$$

with μ_0 being the permeability of free space, $\vec{m}$ the magnetic dipole moment, and r the absolute value of the corresponding position vector $\vec{r}$. In Cartesian coordinates, the three components of the magnetic field are:

$$B_x = \frac{\mu_0}{4\pi}\frac{3xz}{r^5} \tag{4.10}$$

$$B_y = \frac{\mu_0}{4\pi}\frac{3yz}{r^5} \tag{4.11}$$

$$B_z = \frac{\mu_0}{4\pi}\frac{(3z^2 - r^2)}{r^5} \tag{4.12}$$

Cosmic rays can reach and interact with the magnetic field from every possible pitch angle and kinetic energy is dependent on the corresponding energy spectrum.

In order for our program to run in a stable way and to avoid unphysical regions due to numerical limitations, we implemented certain restrictions and features: We code the hit of a particle with the cube by "1" and the missing deflection/capture by "0". With the cube-shaped detecting unit being centralized around the coordinate origin with a side-length of 10 cm. The magnetic dipole field also originates at the origin and is scaled so that we have an effective strength of 10 Tesla on the surface of the detecting unit. Due to the assumption that there is no electric field in the close vicinity of the telescope we require the velocity to remain constant. Due to the numerical precision of the highly relativistic particle it can happen that a specific forward jump in time results in a superluminal motion, which we flag in the simulation. The speed of light is added as the natural upper bound for all massive particles to preserve causality. Figure 4.1 shows some trajectories of a 1 MeV proton in a 10 T magnetic field with the green trajectories indicating the proton passing by the detector and red trajectories colliding with the detector. Here the cube-shaped detecting unit is indicated by the black box. The magnetic dipole field is located at the origin and engulfs the detecting unit with a surface field strength of 10 T. The shown trajectories should indicate the implemented variance along the x-coordinate. In principle, one would need to simulate a plane particle beam from infinity to the detector so that all different pitch angles are tested. Because we are testing many different particles and energies, a plane beam on a surrounding sphere is computationally too intensive. For this reason, we test 5 initial angles from a grid of positions around a sphere of 0.75 m. We tested initial azimuthal angles from 1.5 ° to 358.5 ° in 3 ° steps. The polar angles started at 0.75 ° and ended at 179.25 ° in 1.5 ° steps. The grid therefore is 120x120 pixels.

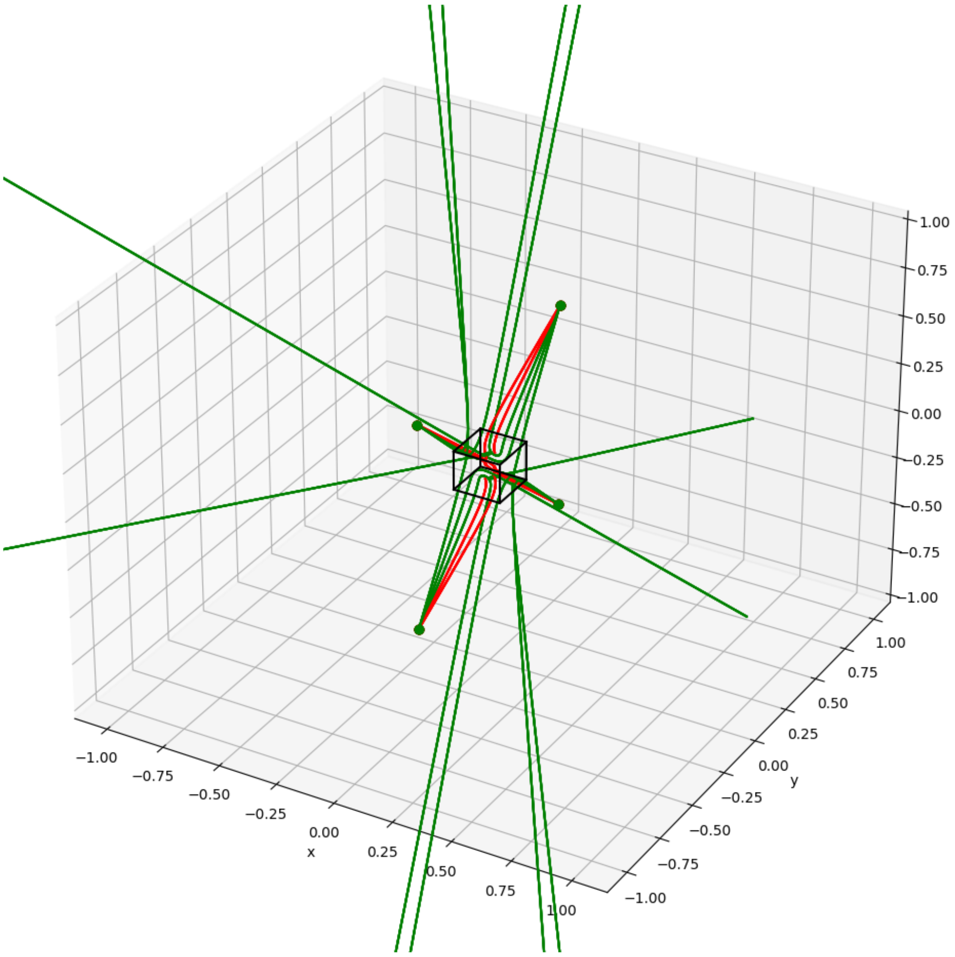

Figure 4.1: A 1 MeV proton is interacting with the 10 T magnetic dipole field around the detector from four different directions. The green trajectories indicate the magnetic field deflected the cosmic rays enough to pass the detector. The red trajectories show the cosmic rays hit the detector and interacted with the components.

Figure 4.2 shows an example trajectory with the deviation along the z-axis instead of the deviation along the x-axis, like we used in the main simulations for this thesis. In this case the 1 MeV proton interacts with the magnetic dipole field centered at the origin with 10 T strength so that it only collides for the radially inward trajectory, while the other trajectories can be deflected above or below the cube-shaped detector.

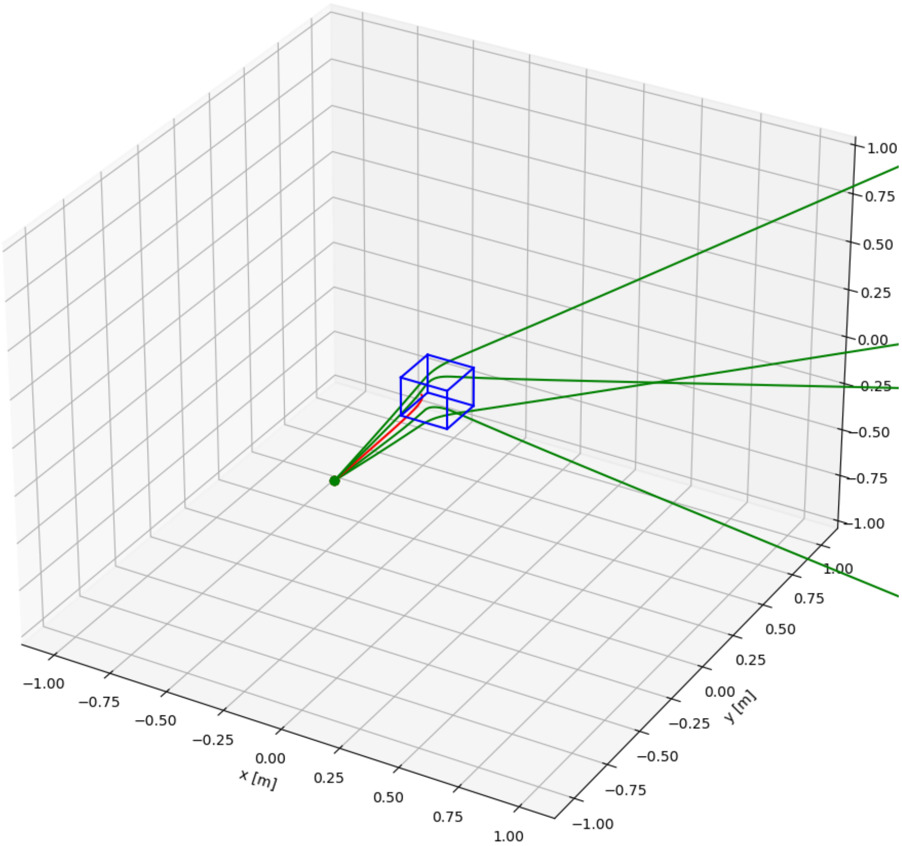

Figure 4.2: A 1 MeV proton is interacting with the 10 T magnetic dipole field around the detector with four different trajectories along the z-axis. The green trajectories indicate the magnetic field deflected the cosmic ray enough to pass the detector. The red trajectories show the cosmic ray hit the detector and interacted with the components.

5 Results

To evaluate how good the shielding method works, we have to calculate the trajectories from all incident angles around the sphere for the electron, proton and the helium nucleus. Because the cosmic rays have a spectrum of energies we are going to simulate energies of 0.1 MeV, 1 MeV, 10 MeV and 100 MeV for all three particles, because we are interested in the bremsstrahlung and cosmic-ray excitation. Cosmic rays excitation is from electrons up to 10 GeV and from protons up to 100 MeV. The spectrum follows a power-law, so it is sufficient to simulate in decade steps and interpolate the data. The resulting SkyMap will indicate where the particles are hitting the detector and where they pass the detector entirely. In our case a SkyMap color codes detected events or misses onto a 2D grid to visualize the results from our simulation. In addition we implemented a deviation along the x-axis of -10 °, -5 °, 5 ° and 10 ° to compare the results to the original radially inward trajectory.

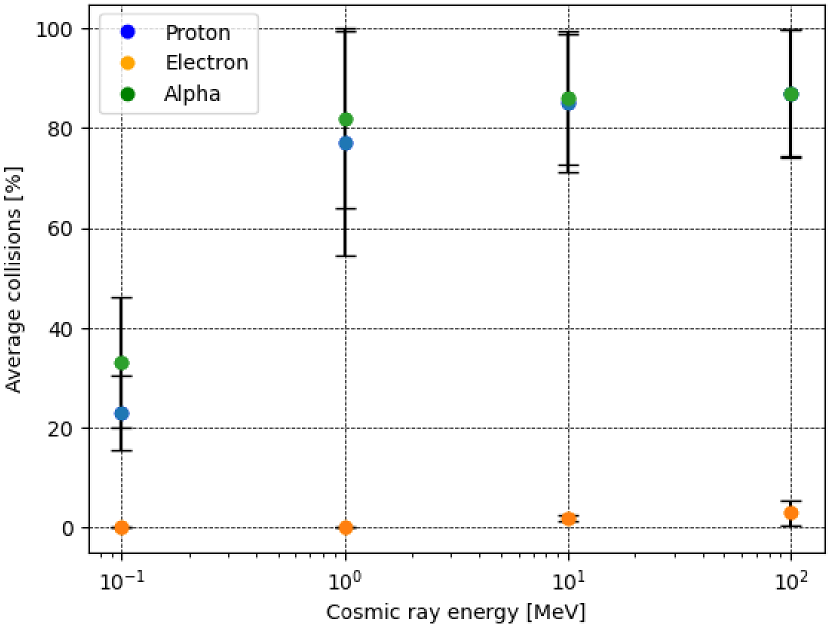

Figure 5.1: The plot show the average collisions of the cosmic rays (proton, electron and alpha-particles) with the detector for the chosen energies of 0.1 MeV, 1 MeV, 10 MeV and 100 MeV.

The SkyMap in figure 5.3 (c) shows that the proton of 1 MeV kinetic energy only gets deflected away from the detector when it approaches the cube-shaped detector from the edges, indicated by the purple region, while the trajectory perpendicular to the surfaces are impacting the device. The SkyMaps of the electrons, seen in figure 5.4, show that the electrons and therefore also the positrons in figure 5.8 only collide with the detector from the pole regions due to their smaller mass than protons and helium nuclei and therefore larger Lorentz force. SkyMaps from helium nuclei from figure 5.5 show that the impact region is broader than the proton impact region due to the higher mass and therefore weaker Lorentz force. Figure 5.6 indicates the impact of varying the magnetic field strength of the dipole field, here doubling from 10 T to 20 T, on the counted collision events. The average collisions of 1 MeV protons are reduced to 36,4% from 76,9% by doubling the magnetic field strength. Because the simulated SkyMaps are linear and therefore every pixel equally weighted, weighting the pixels at the pole regions differently than the equatorial regions would be more appropriate due the symmetry of the system, results in different collision percentages, for example 14% instead of 56,1% in the case of figure 5.6 (e). Figure 5.7 shows the charge inversion from a proton to an anti-proton at 1 MeV kinetic energy which resulted in a mirrored SkyMap, indicated by figure 5.6 (e) and figure 5.7 (a).

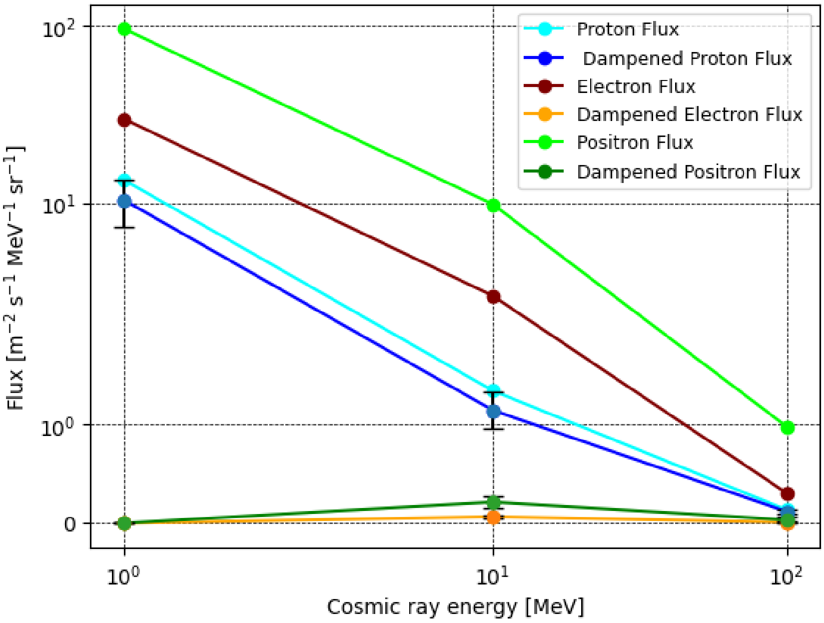

Figure 5.2: The plot shows the initial flux from secondary electrons, positrons and protons from figure 1.2 and compares them to the expected dampened spectrum arising from our simulations.

The results from our simulations in figure 5.1 are now applied to figure 1.2 to compare the original flux from the secondary electrons, positrons and protons to the expected dampened flux due to the magnetic shielding of the cube-shaped detector unit, shown in figure 5.2. The flux from electrons and positrons is dampened significantly while the protons are slightly dampened.

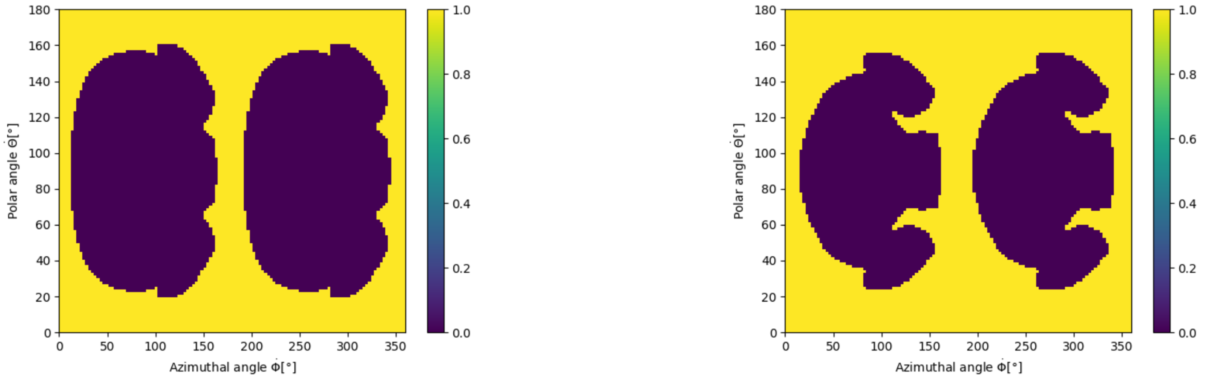

(a) The SkyMap of a 1 MeV proton with a deviation of -10 ° resulted in 6344 (44,1%) hits from 14400 simulated trajectories.

(b) The SkyMap of a 1 MeV proton with a deviation of -5 ° resulted in 8164 (56,7%) hits from 14400 simulated trajectories.

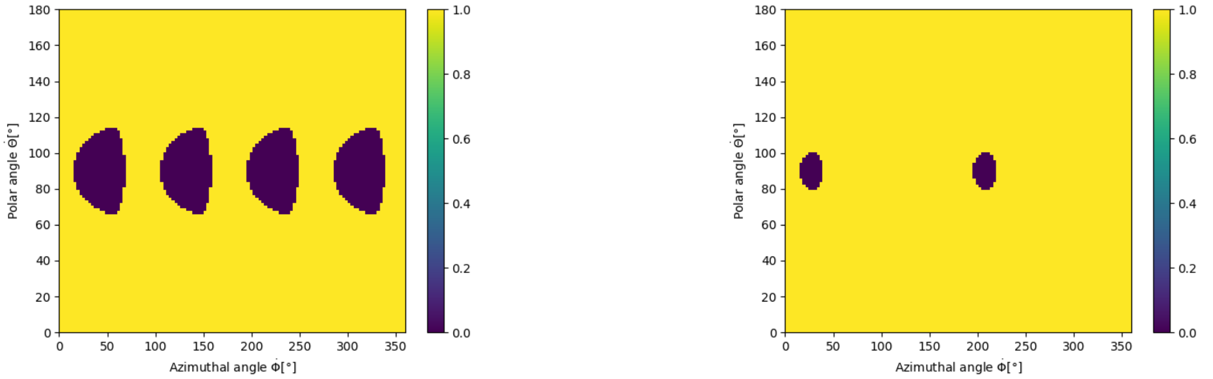

(c) The SkyMap of a 1 MeV proton with a radially inward trajectory resulted in 12632 (87,7%) hits from 14400 simulated trajectories.

(d) The SkyMap of a 1 MeV proton with a deviation of 5 ° resulted in 14220 (98,75%) hits from 14400 simulated trajectories.

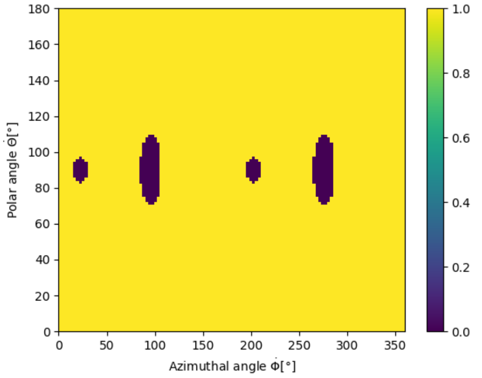

(e) The SkyMap of a 1 MeV proton with a deviation of 10 ° resulted in 14024 (97,4%) hits from 14400 simulated trajectories.

Figure 5.3: The five simulated SkyMaps show at which incident angles around the sphere the 1 MeV proton interacts with the detector indicated with the value ”1” and the proton passes by the detector with the value ”0”.

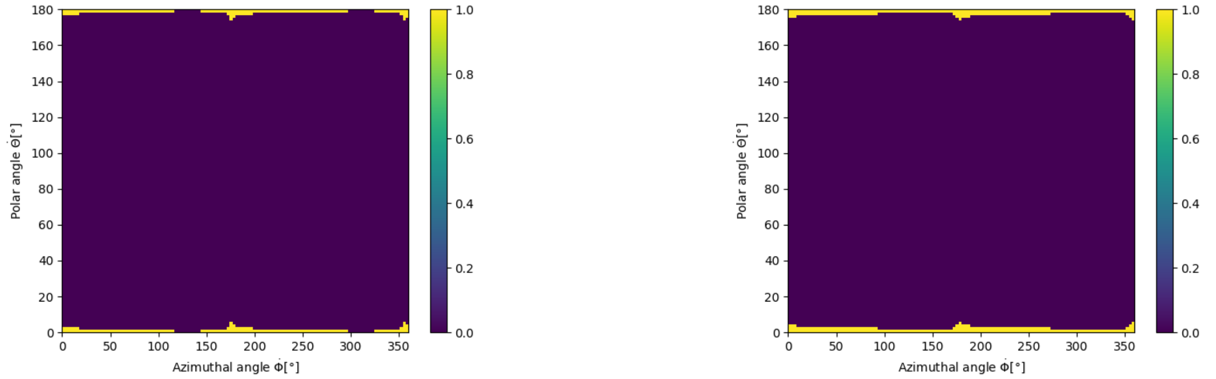

(a) The SkyMap of a 100 MeV electron with a deviation of -10 ° resulted in 252 (1,8%) hits from 14400 simulated trajectories.

(b) The SkyMap of a 100 MeV electron with a deviation of -5 ° resulted in 400 (2,8%) hits from 14400 simulated trajectories.

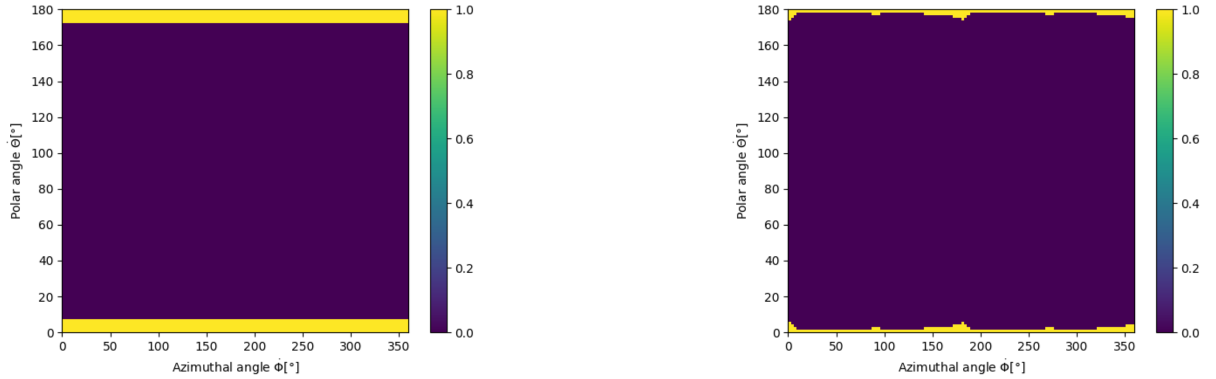

(c) The SkyMap of a 100 MeV electron with a radially inward trajectory resulted in 1200 (8,3%) hits from 14400 simulated trajectories.

(d) The SkyMap of a 100 MeV electron with a deviation of 5 ° resulted in 340 (2,4%) hits from 14400 simulated trajectories.

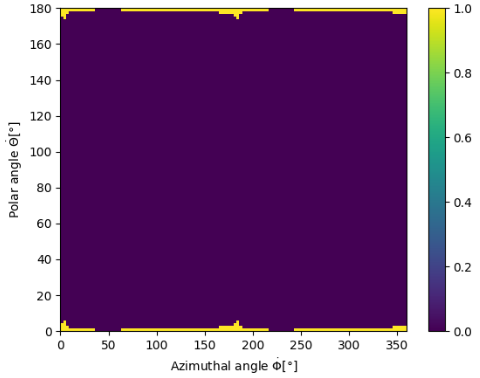

(e) The SkyMap of a 100 MeV electron with a deviation of 10 ° resulted in 248 (1,7%) hits from 14400 simulated trajectories.

Figure 5.4: The five simulated SkyMaps show at which incident angles around the sphere the 100 MeV electron interacts with the detector indicated with the value "1" and the electron passes by the detector with the value "0".

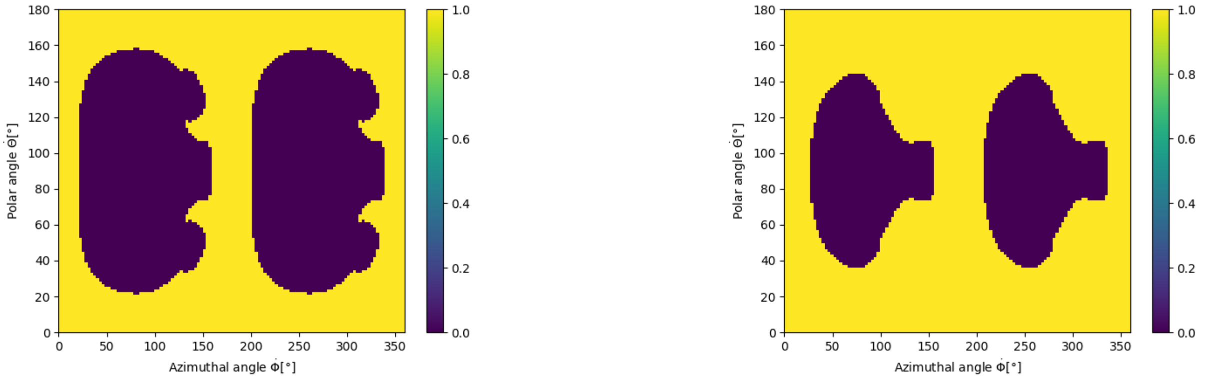

(a) The SkyMap of a 1 MeV helium nucleus with a deviation of -10 ° resulted in 7416 (51,5%) hits from 14400 simulated trajectories.

(b) The SkyMap of a 1 MeV helium nucleus with a deviation of -5 ° resulted in 10376 (72,1%) hits from 14400 simulated trajectories.

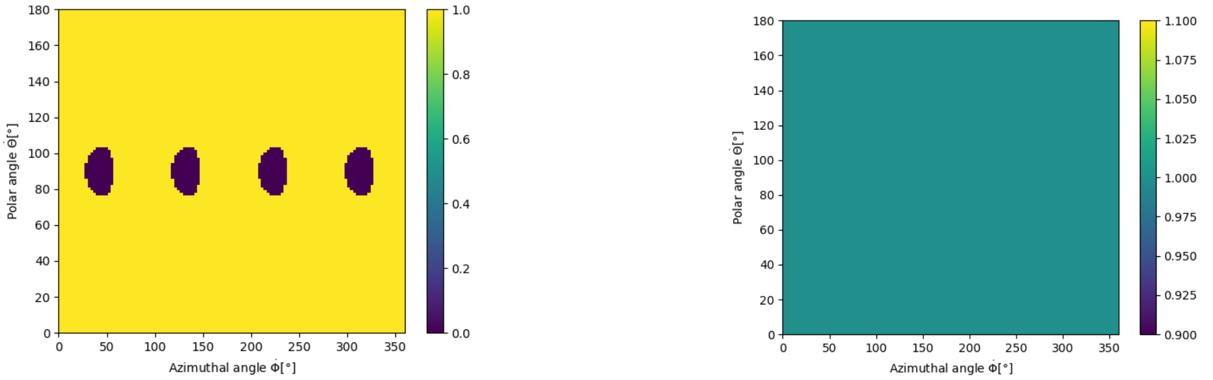

(c) The SkyMap of a 1 MeV helium nucleus with a radially inward trajectory resulted in 13816 (95,9%) hits from 14400 simulated trajectories.

(d) The SkyMap of a 1 MeV helium nucleus with a deviation of 5 ° resulted in 14400 (100%) hits from 14400 simulated trajectories.

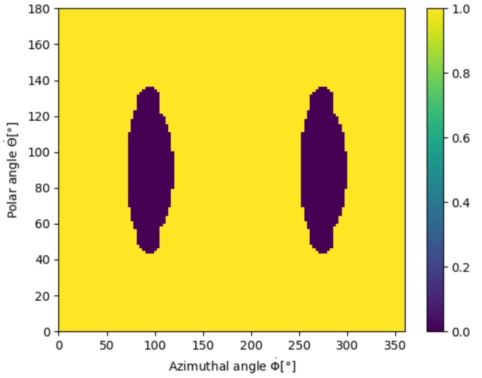

(e) The SkyMap of a 1 MeV helium nucleus with a deviation of 10 ° resulted in 12908 (89,6%) hits from 14400 simulated trajectories.

Figure 5.5: The five simulated SkyMaps show at which incident angles around the sphere the 1 MeV helium nucleus interacts with the detector indicated with the value ”1” and the helium nucleus passes by the detector with the value ”0”.

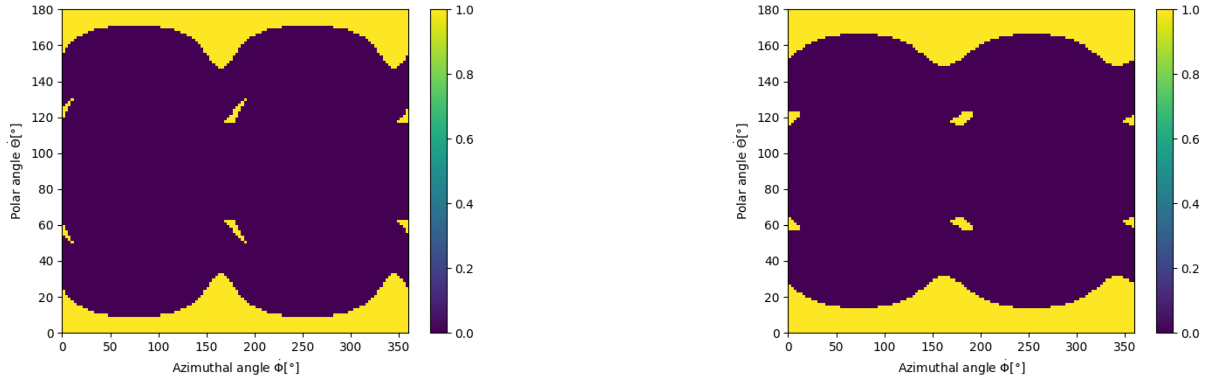

(a) The SkyMap of a 1 MeV proton in a 20 T magnetic dipole field with a deviation of -10 ° resulted in 2548 (17,7%) hits from 14400 simulated trajectories.

(b) The SkyMap of a 1 MeV proton in a 20 T magnetic dipole field with a deviation of -5 ° resulted in 3276 (22,8%) hits from 14400 simulated trajectories.

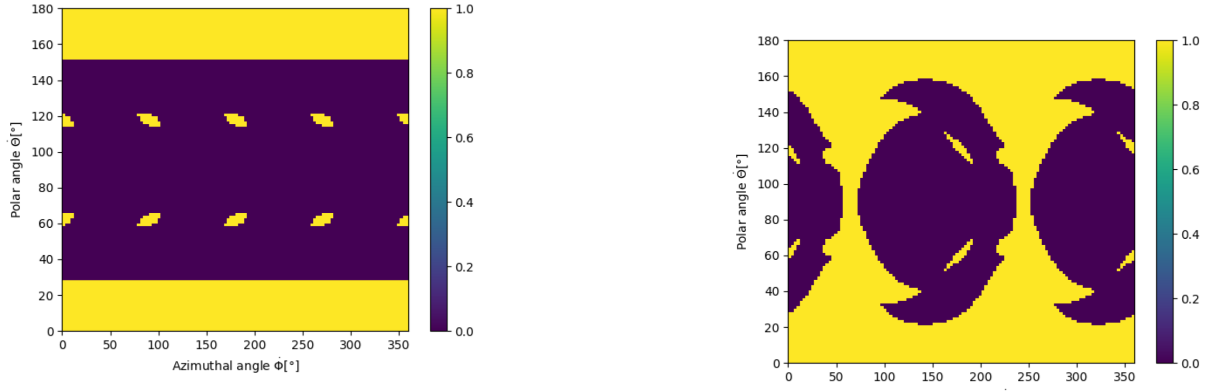

(c) The SkyMap of a 1 MeV proton in a 20 T magnetic dipole field with a radially inward trajectory resulted in 4776 (33,2%) hits from 14400 simulated trajectories.

(d) The SkyMap of a 1 MeV proton in a 20 T magnetic dipole field with a deviation of 5 ° resulted in 7504 (52,1%) hits from 14400 simulated trajectories.

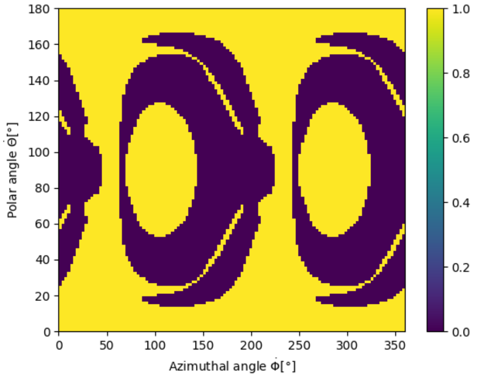

(e) The SkyMap of a 1 MeV proton in a 20 T magnetic dipole field with a deviation of 10 ° resulted in 8080 (56,1%) hits from 14400 simulated trajectories.

Figure 5.6: The five simulated SkyMaps show at which incident angles around the sphere the 1 MeV proton in a 20 T magnetic dipole field interacts with the detector indicated with the value "1" and the proton passes by the detector with the value "0".

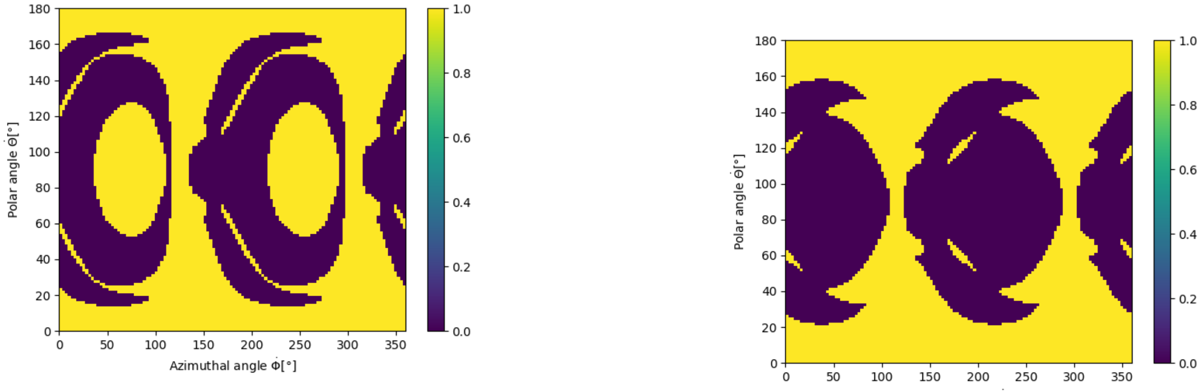

(a) The SkyMap of a 1 MeV anti-proton in a 20 T magnetic dipole field with a deviation of -10 ° resulted in 8080 (56,1%) hits from 14400 simulated trajectories.

(b) The SkyMap of a 1 MeV anti-proton in a 20 T magnetic dipole field with a deviation of -5 ° resulted in 7504 (52,1%) hits from 14400 simulated trajectories.

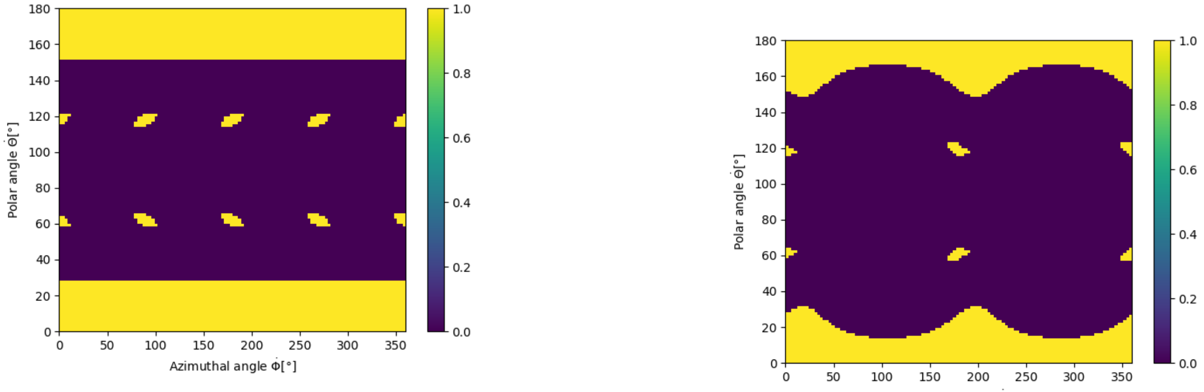

(c) The SkyMap of a 1 MeV anti-proton in a 20 T magnetic dipole field with a radially inward trajectory resulted in 4776 (33,2%) hits from 14400 simulated trajectories.

(d) The SkyMap of a 1 MeV anti-proton in a 20 T magnetic dipole field with a deviation of 5 ° resulted in 3276 (22,8%) hits from 14400 simulated trajectories.

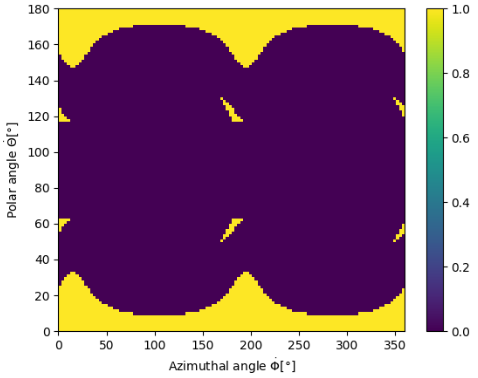

(e) The SkyMap of a 1 MeV anti-proton in a 20 T magnetic dipole field with a deviation of 10 ° resulted in 2548 (17,7%) hits from 14400 simulated trajectories.

Figure 5.7: The five simulated SkyMaps show at which incident angles around the sphere the 1 MeV anti-proton in a 20 T magnetic dipole field interacts with the detector indicated with the value ”1” and the anti-proton passes by the detector with the value ”0”.

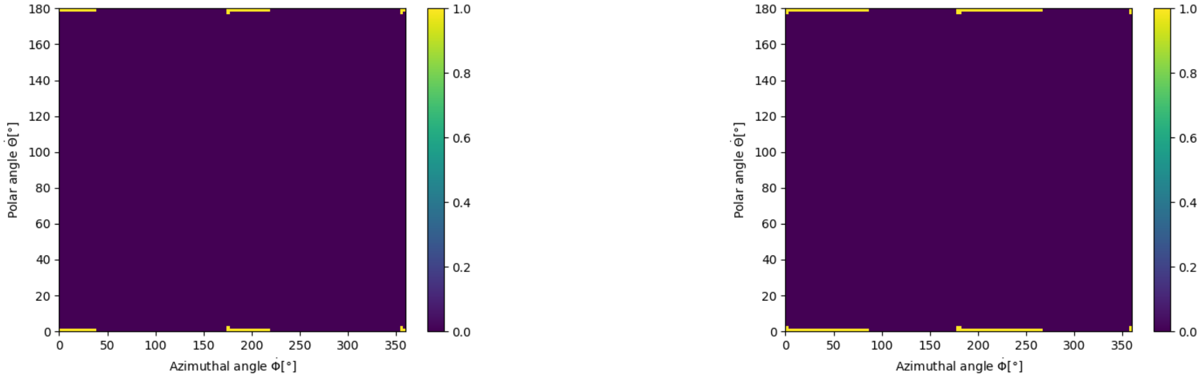

(a) The SkyMap of a 1 GeV positron with a deviation of -10 ° resulted in 64 (0,4%) hits from 14400 simulated trajectories.

(b) The SkyMap of a 1 GeV positron with a deviation of -5 ° resulted in 128 (0,9%) hits from 14400 simulated trajectories.

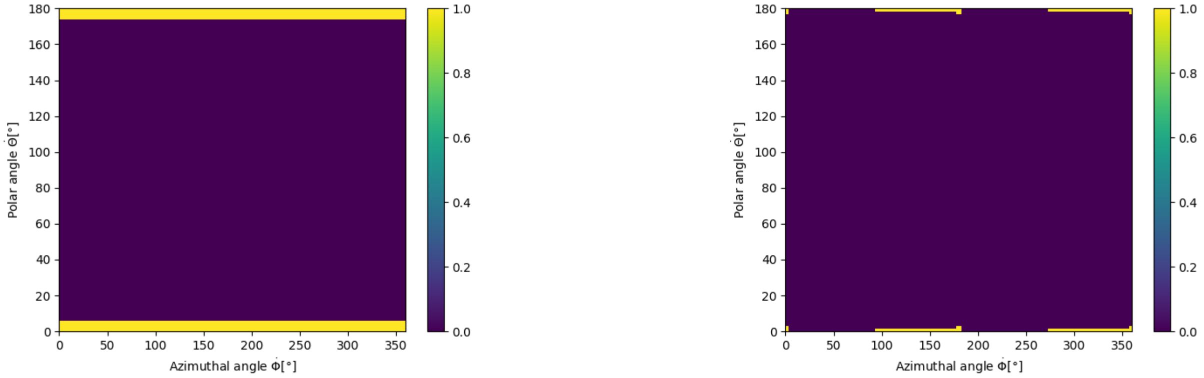

(c) The SkyMap of a 1 GeV positron with a radially inward trajectory resulted in 960 (6,7%) hits from 14400 simulated trajectories.

(d) The SkyMap of a 1 GeV positron with a deviation of 5 ° resulted in 128 (0,9%) hits from 14400 simulated trajectories.

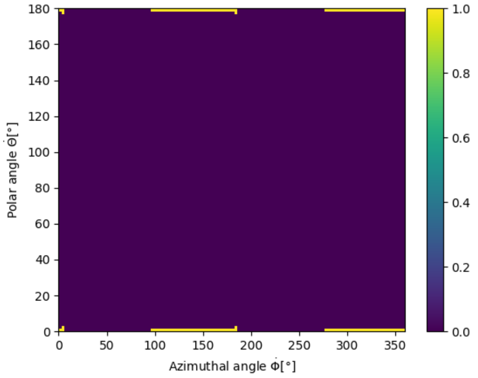

(e) The SkyMap of a 1 GeV positron with a deviation of 10 ° resulted in 124 (0,9%) hits from 14400 simulated trajectories.

Figure 5.8: The five simulated SkyMaps show at which incident angles around the sphere the 1 GeV positron interacts with the detector indicated with the value "1" and the positron passes by the detector with the value "0".

6 Conclusion & Outlook

Given our simulation setup, consisting of a 100% efficient cube-shaped detecting unit, side length of 10 cm, that is bombarded with cosmic rays of 0.1 MeV, 1 MeV, 10 MeV and 100 MeV surrounded by a 10 T magnetic dipole field, we find that 13.4% to 23.1% of the incoming proton flux would be deflected. For electrons we find that 96.6% to 100% of incoming flux and for positrons 96.6% to 100% of incoming flux would be deflected. This leads to the conclusion that this configuration is most efficient for lighter cosmic rays like electrons and positrons. Because the magnetic shield is intended to completely replace the ACS even the relatively low collision percentages for lighter particles can be very harmful for the components and electronics. The higher energy cosmic rays are almost exclusively impacting onto the detector and could be barely deflected, however, their contribution to the total measured background radiation is significantly lower above 10 MeV.
We suggest that a magnetic dipole field is not sufficient for the purpose of a magnetic shield for gamma-ray telescopes, but that there is a chance to find a optimized and suitable magnetic shield configuration. Instead of just relying on the pure strength of the magnetic field to exert a large enough Lorentz force on the charged particles, other concepts, like scattering of irregularities in a magnetic field, similar to total reflection off a surface.

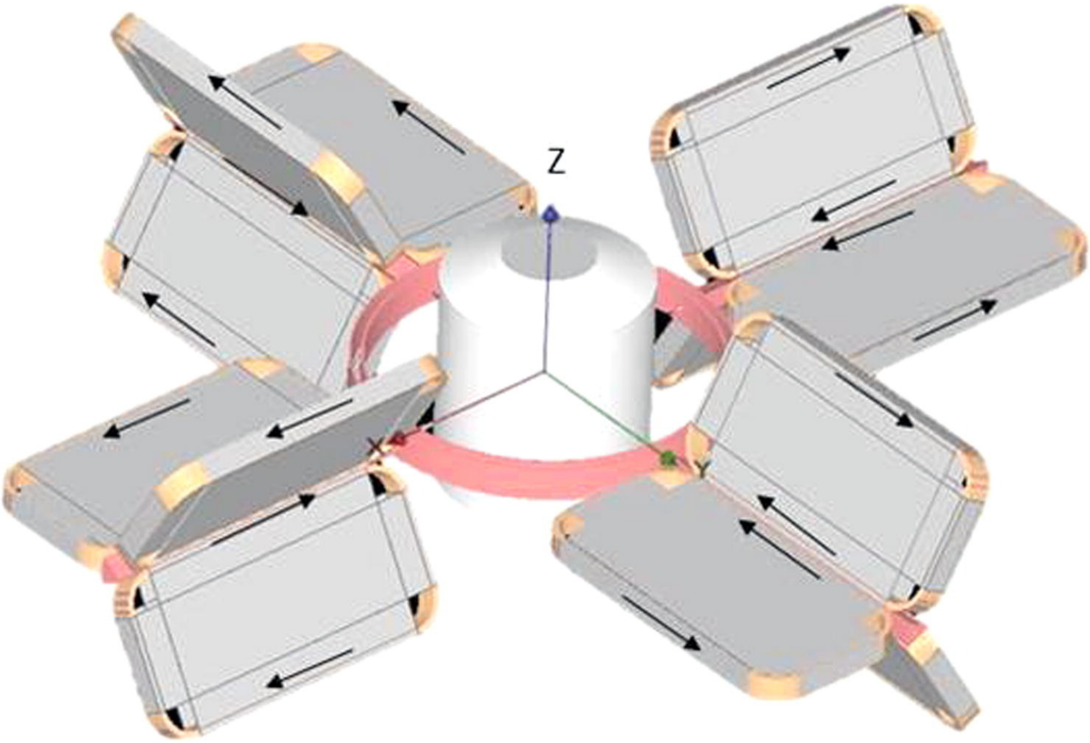

Figure 6.1: The ”Pumpkin configuration”, a multiple toroid magnet system with 3 racetrack coils each [Al Zaman et al.(2021)].

The magnetic shield configuration in figure 6.1 and other toroidal strutures have been proposed for human space voyages to protect the habitable zone of the spacecraft from harmful cosmic rays for living organisms [Al Zaman et al.(2021)]. In more advanced simulations these configurations can be tested and improved upon, to allow further advances in human spaceflight and more effective shielding of space based instruments.

Bibliography

[Al Zaman et al.(2021)] Md. Abdullah Al Zaman, H.M.A.R. Maruf, M.R. Islam, Neelufar Panna, Study on superconducting magnetic shield for the manned long termed space voyages, The Egyptian Journal of Remote Sensing and Space Science, Volume 24, Issue 2, 2021, p.203-210

[Siegert et al.(2022)] Siegert, T., Horan, D., Kanbach, G. 2022. Telescope Concepts in Gamma-Ray Astronomy. Handbook of X-ray and Gamma-ray Astrophysics. doi:10.1007/978-981-16-4544-0_43-1

[Schanne et al.(2003] Stéphane Schanne, B. Cordier, M. Gros, D. Attié, P. v. Ballmoos, L. Bouchet, R. Carli, P. Connell, R. Diehl, P. Jean, J. Kiener, A. v. Kienlin, J. Knödlseder, P. Laurent, G. Lichti, P. Mandrou, J. Paul, P. Paul, J.-P. Roques, F. Sanchez, V. Schönfelder, C. Shrader, G. Skinner, A. Strong, S. Sturner, V. Tatischeff, B. Teegarden, G. Vedrenne, G. Weidenspointner, C. Wunderer 2003. Calibration of the Spectrometer aboard the INTEGRAL satellite. doi.org/10.48550/arXiv.astro-ph/0310792

[Cumani et al.(2019)] Cumani, P., Hernanz, M., Kiener, J., Tatischeff, V., Zoglauer, A. 2019. Background for a gamma-ray satellite on a low-Earth orbit. Experimental Astronomy 47, 273–302. doi:10.1007/s10686-019-09624-0

[von Kienlin et al.(2003)] von Kienlin, A. and 18 colleagues 2003. INTEGRAL Spectrometer SPI's GRB detection capabilities. GRBs detected inside SPI's FoV and with the anticoincidence system ACS. Astronomy and Astrophysics 411, L299–L305. doi:10.1051/0004-6361:20031231

[Diehl et al.(2018)] Diehl, R. and 9 colleagues 2018. INTEGRAL/SPI γ-ray line spectroscopy. Response and background characteristics. Astronomy and Astrophysics 611. doi:10.1051/0004-6361/201731815

[1] Matthias Bartelmann, Björn Feuerbacher, Timm Krüger, Dieter Lüst, Anton Rebhan, Andreas Wipf (2015). Theoretische Physik. Springer Spektrum. Berlin, Heidelberg: p. 400

[2] Malcolm S. Longair (2014). High Energy Astrophysics (Third Edition). Cambridge University Press. Cambridge: p. 178 - 203

[3] Runge-Kutta Methods, University of Münster Lectures, 2016 https://www.uni-muenster.de/imperia/md/content/physik_tp/lectures/ss2016/num_methods_ii/rkm.pdf

Appendix

The following figures 6.2 - 6.7 show the python program used for the simulations of the SkyMaps. Figure 6.2 defines the classes fro the three different numerical methods (Forward Euler, Explicit Midpoint and Runge-Kutta-4) with the equations 4.1, 4.2 and 4.7 respectively.

The initial conditions for the starting point, particle mass and charge, numerical method, as well as starting velocity for the simulations are shown in figure 6.3.

The chosen magnetic field as a continuous variable for the Lorentz force used in the simulations can be implemented, scaled and adjusted as shown in figure 6.4.

The differential equation solver in figure 6.5 uses the initial conditions for velocity, charge and mass of the particle and the value of the magnetic field strength to calculate the next iteration steps according to the chosen numerical method.

To account for the physical conditions like the location of the cube-shaped detecting unit, the allowed deviation from the initial velocity or sub-lightspeed propagation of massive particles, we implemented flagging conditions that filter out unphysical results in figure 6.6.

Figure 6.7 shows the multiprocessing function that allows use to utilize more CPU cores to reduce computational time for multiple for-loops.

The figures 6.8 to 6.16 are the additional SkyMaps from the simulations for the protons, electrons and helium nuclei. Figures 6.17 and 6.18 are example trajectories from 10 MeV electron and positron simulations to visualize how they collide at the pole regions.

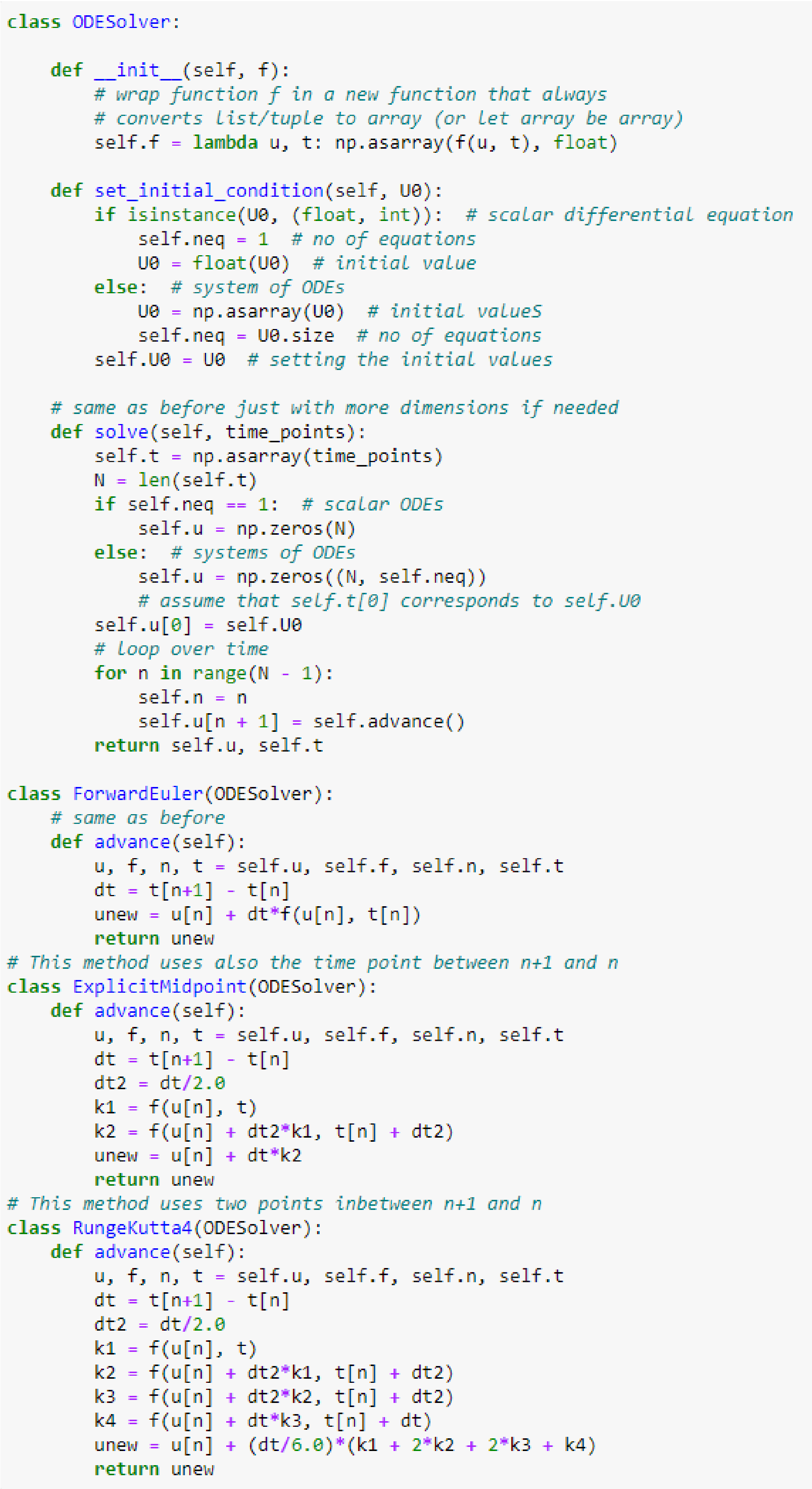

```
class ODESolver:

    def __init__(self, f):
        # wrap function f in a new function that always
        # converts list/tuple to array (or let array be array)
        self.f = lambda u, t: np.asarray(f(u, t), float)

    def set_initial_condition(self, U0):
        if isinstance(U0, (float, int)):  # scalar differential equation
            self.neq = 1  # no of equations
            U0 = float(U0)  # initial value
        else:  # system of ODEs
            U0 = np.asarray(U0)  # initial valueS
            self.neq = U0.size  # no of equations
        self.U0 = U0  # setting the initial values

    # same as before just with more dimensions if needed
    def solve(self, time_points):
        self.t = np.asarray(time_points)
        N = len(self.t)
        if self.neq == 1:  # scalar ODEs
            self.u = np.zeros(N)
        else:  # systems of ODEs
            self.u = np.zeros((N, self.neq))
            # assume that self.t[0] corresponds to self.U0
        self.u[0] = self.U0
        # loop over time
        for n in range(N - 1):
            self.n = n
            self.u[n + 1] = self.advance()
        return self.u, self.t

class ForwardEuler(ODESolver):
    # same as before
    def advance(self):
        u, f, n, t = self.u, self.f, self.n, self.t
        dt = t[n+1] - t[n]
        unew = u[n] + dt*f(u[n], t[n])
        return unew
# This method uses also the time point between n+1 and n
class ExplicitMidpoint(ODESolver):
    def advance(self):
        u, f, n, t = self.u, self.f, self.n, self.t
        dt = t[n+1] - t[n]
        dt2 = dt/2.0
        k1 = f(u[n], t)
        k2 = f(u[n] + dt2*k1, t[n] + dt2)
        unew = u[n] + dt*k2
        return unew
# This method uses two points inbetween n+1 and n
class RungeKutta4(ODESolver):
    def advance(self):
        u, f, n, t = self.u, self.f, self.n, self.t
        dt = t[n+1] - t[n]
        dt2 = dt/2.0
        k1 = f(u[n], t)
        k2 = f(u[n] + dt2*k1, t[n] + dt2)
        k3 = f(u[n] + dt2*k2, t[n] + dt2)
        k4 = f(u[n] + dt*k3, t[n] + dt)
        unew = u[n] + (dt/6.0)*(k1 + 2*k2 + 2*k3 + k4)
        return unew
```

Figure 6.2: Ordinary differential equation solver to execute the numerical methods described in chapter 4.1.

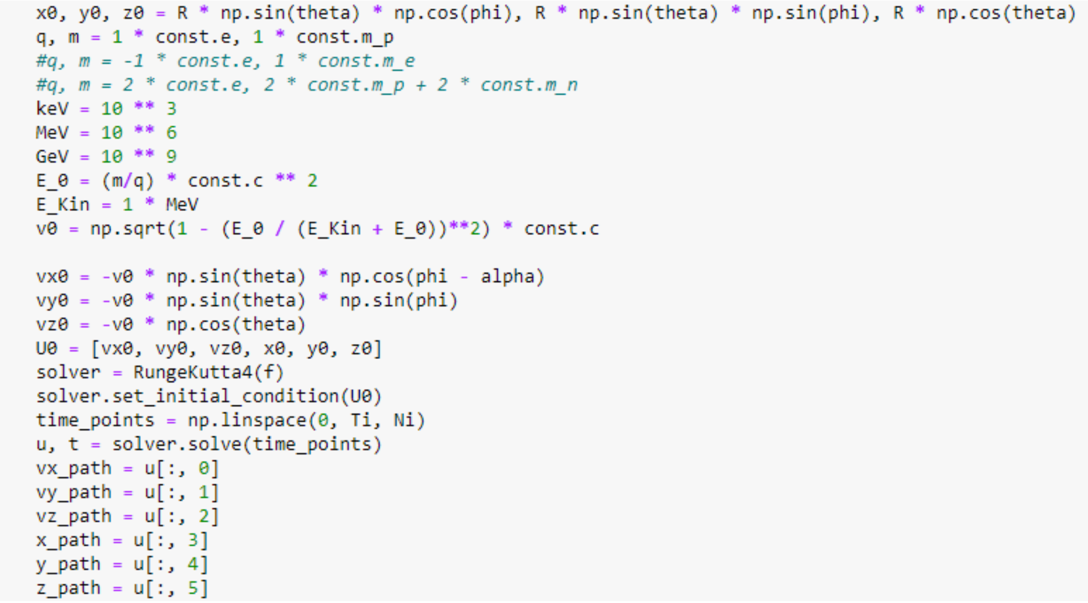

```
x0, y0, z0 = R * np.sin(theta) * np.cos(phi), R * np.sin(theta) * np.sin(phi), R * np.cos(theta)
q, m = 1 * const.e, 1 * const.m_p
#q, m = -1 * const.e, 1 * const.m_e
#q, m = 2 * const.e, 2 * const.m_p + 2 * const.m_n
keV = 10 ** 3
MeV = 10 ** 6
GeV = 10 ** 9
E_0 = (m/q) * const.c ** 2
E_Kin = 1 * MeV
v0 = np.sqrt(1 - (E_0 / (E_Kin + E_0))**2) * const.c

vx0 = -v0 * np.sin(theta) * np.cos(phi - alpha)
vy0 = -v0 * np.sin(theta) * np.sin(phi)
vz0 = -v0 * np.cos(theta)
U0 = [vx0, vy0, vz0, x0, y0, z0]
solver = RungeKutta4(f)
solver.set_initial_condition(U0)
time_points = np.linspace(0, Ti, Ni)
u, t = solver.solve(time_points)
vx_path = u[:, 0]
vy_path = u[:, 1]
vz_path = u[:, 2]
x_path = u[:, 3]
y_path = u[:, 4]
z_path = u[:, 5]
```

Figure 6.3: Initial conditions for the starting point, particle mass and charge, numerical method, as well as starting velocity.

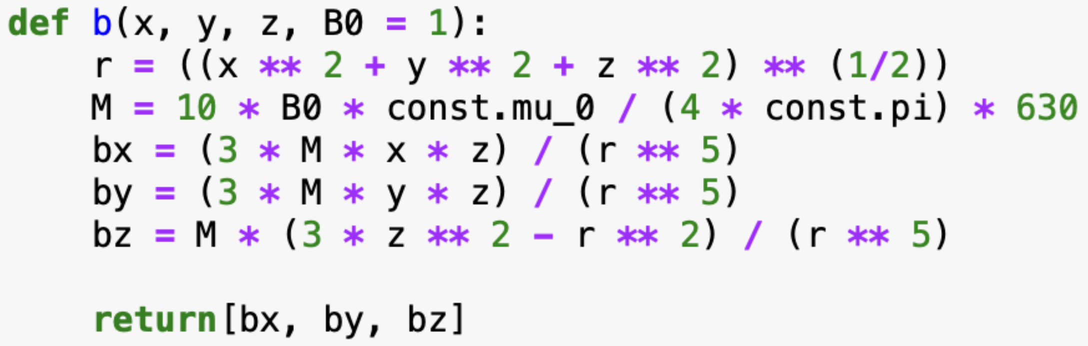

```
def b(x, y, z, B0 = 1):
    r = ((x ** 2 + y ** 2 + z ** 2) ** (1/2))
    M = 10 * B0 * const.mu_0 / (4 * const.pi) * 630
    bx = (3 * M * x * z) / (r ** 5)
    by = (3 * M * y * z) / (r ** 5)
    bz = M * (3 * z ** 2 - r ** 2) / (r ** 5)

    return[bx, by, bz]
```

Figure 6.4: This image shows how the magnetic field can be implemented into the code. For our specific case, we chose a magnetic dipole field with r being the position vector, and M the magnetic dipole moment with a scaling factor to match our initial condition of $B = 10\,T$ on the surface of the satellite. Bx, By and Bz are the cartesian components (Equations 4.10-4.12) of the magnetic field from its form in Equation 4.9.

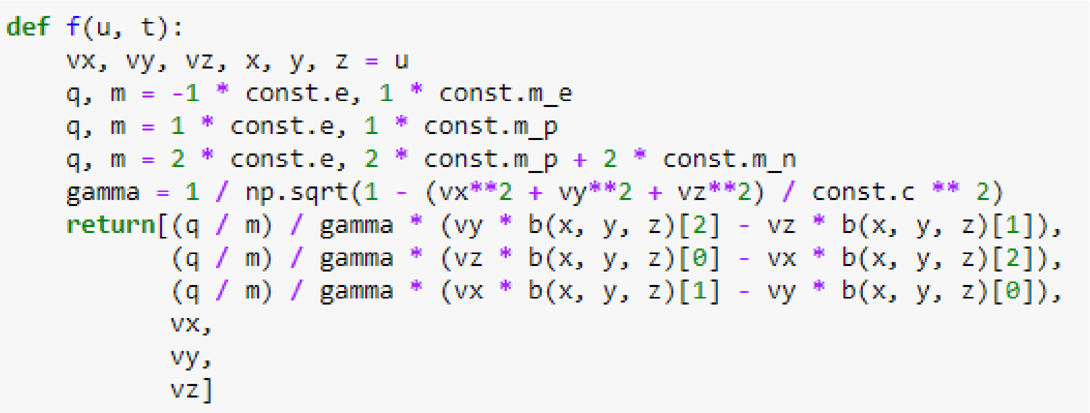

```
def f(u, t):
    vx, vy, vz, x, y, z = u
    q, m = -1 * const.e, 1 * const.m_e
    q, m = 1 * const.e, 1 * const.m_p
    q, m = 2 * const.e, 2 * const.m_p + 2 * const.m_n
    gamma = 1 / np.sqrt(1 - (vx**2 + vy**2 + vz**2) / const.c ** 2)
    return[(q / m) / gamma * (vy * b(x, y, z)[2] - vz * b(x, y, z)[1]),
           (q / m) / gamma * (vz * b(x, y, z)[0] - vx * b(x, y, z)[2]),
           (q / m) / gamma * (vx * b(x, y, z)[1] - vy * b(x, y, z)[0]),
           vx,
           vy,
           vz]
```

Figure 6.5: The differential equation solver for the relativistic Lorentz force.

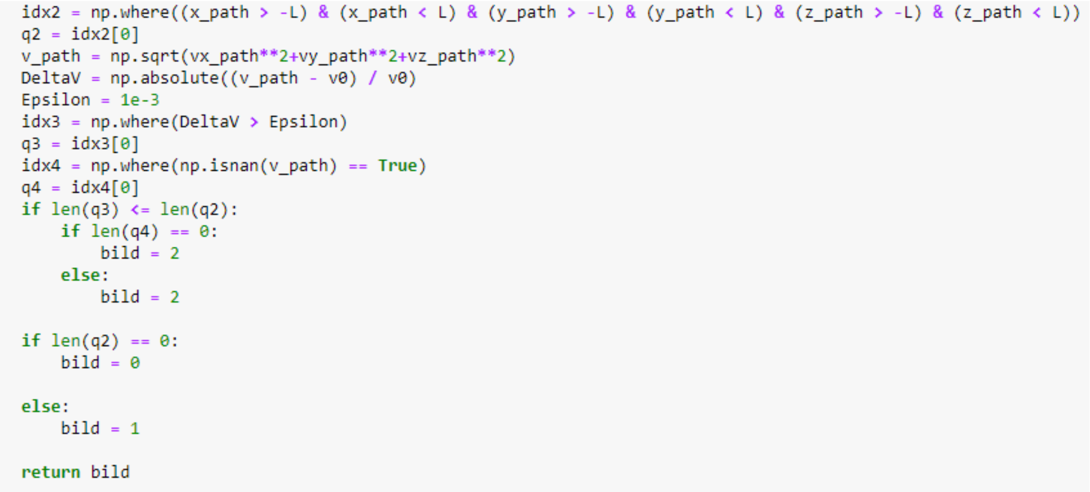

```
idx2 = np.where((x_path > -L) & (x_path < L) & (y_path > -L) & (y_path < L) & (z_path > -L) & (z_path < L))
q2 = idx2[0]
v_path = np.sqrt(vx_path**2+vy_path**2+vz_path**2)
DeltaV = np.absolute((v_path - v0) / v0)
Epsilon = 1e-3
idx3 = np.where(DeltaV > Epsilon)
q3 = idx3[0]
idx4 = np.where(np.isnan(v_path) == True)
q4 = idx4[0]
if len(q3) <= len(q2):
    if len(q4) == 0:
        bild = 2
    else:
        bild = 2

if len(q2) == 0:
    bild = 0

else:
    bild = 1

return bild
```

Figure 6.6: Physical condition for our simulations. Idx2 represents the location of the detector, Idx3 the allowed deviation from the starting velocity as a results of numerical calculations and Idx4 sub-lightspeed propagation of massive particles.

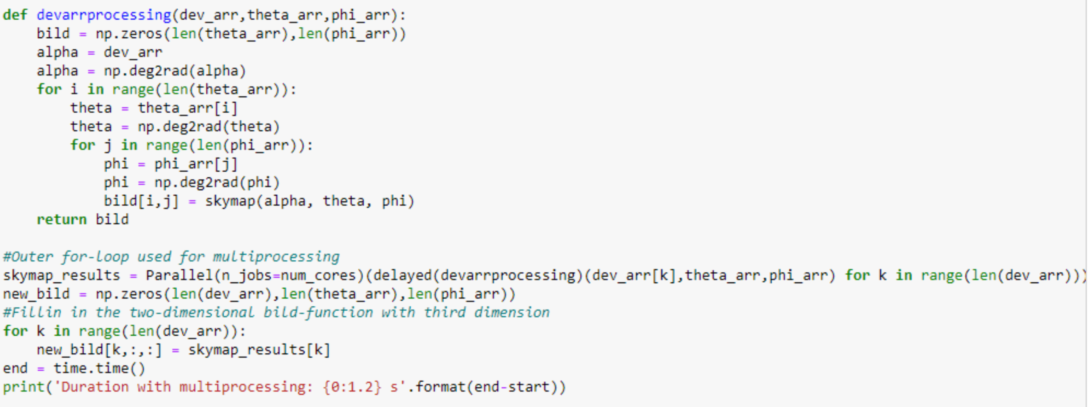

```
def devarrprocessing(dev_arr,theta_arr,phi_arr):
    bild = np.zeros(len(theta_arr),len(phi_arr))
    alpha = dev_arr
    alpha = np.deg2rad(alpha)
    for i in range(len(theta_arr)):
        theta = theta_arr[i]
        theta = np.deg2rad(theta)
        for j in range(len(phi_arr)):
            phi = phi_arr[j]
            phi = np.deg2rad(phi)
            bild[i,j] = skymap(alpha, theta, phi)
    return bild

#Outer for-Loop used for multiprocessing
skymap_results = Parallel(n_jobs=num_cores)(delayed(devarrprocessing)(dev_arr[k],theta_arr,phi_arr) for k in range(len(dev_arr))
new_bild = np.zeros(len(dev_arr),len(theta_arr),len(phi_arr))
#Fillin in the two-dimensional bild-function with third dimension
for k in range(len(dev_arr)):
    new_bild[k,:,:] = skymap_results[k]
end = time.time()
print('Duration with multiprocessing: {0:1.2} s'.format(end-start))
```

Figure 6.7: Implementing the Multiprocessing function into the python program to utilize more CPU cores to reduce computational time

Additional figures

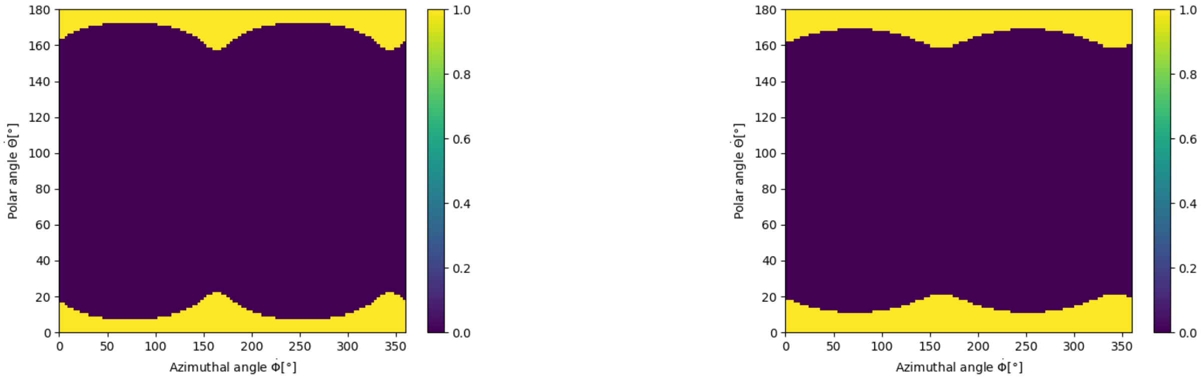

(a) The SkyMap of a 0.1 MeV proton with a deviation of -10 ° resulted in 1916 (13,3%) hits from 14400 simulated trajectories.

(b) The SkyMap of a 0.1 MeV proton with a deviation of -5 ° resulted in 2368 (16,4%) hits from 14400 simulated trajectories.

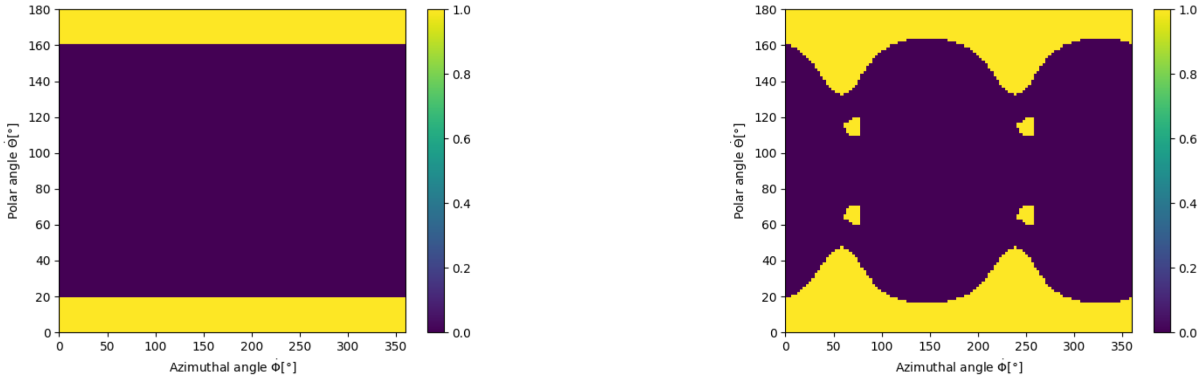

(c) The SkyMap of a 0.1 MeV proton with a radially inward trajectory resulted in 3120 (21,7%) hits from 14400 simulated trajectories.

(d) The SkyMap of a 0.1 MeV proton with a deviation of 5 ° resulted in 4420 (30,7%) hits from 14400 simulated trajectories.

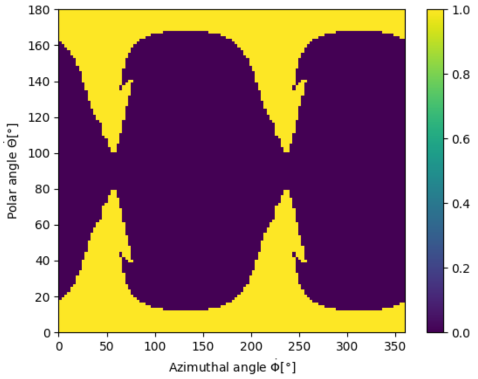

(e) The SkyMap of a 0.1 MeV proton with a deviation of 10 ° resulted in 4548 (31,6%) hits from 14400 simulated trajectories.

Figure 6.8: The five simulated SkyMaps show at which incident angles around the sphere the 0.1 MeV proton interacts with the detector indicated with the value "1" and the proton passes by the detector with the value "0".

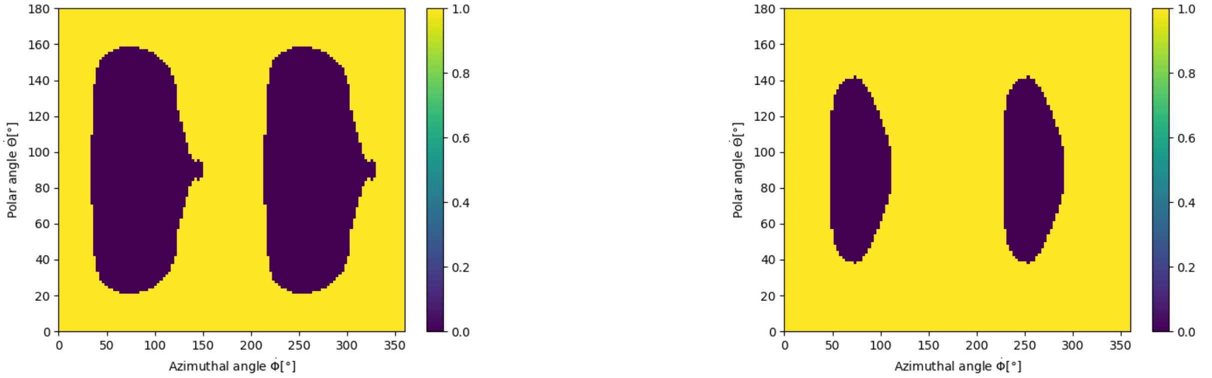

(a) The SkyMap of a 10 MeV proton with a deviation of -10 ° resulted in 9096 (63,2%) hits from 14400 simulated trajectories.

(b) The SkyMap of a 10 MeV proton with a deviation of -5 ° resulted in 12112 (84,1%) hits from 14400 simulated trajectories.

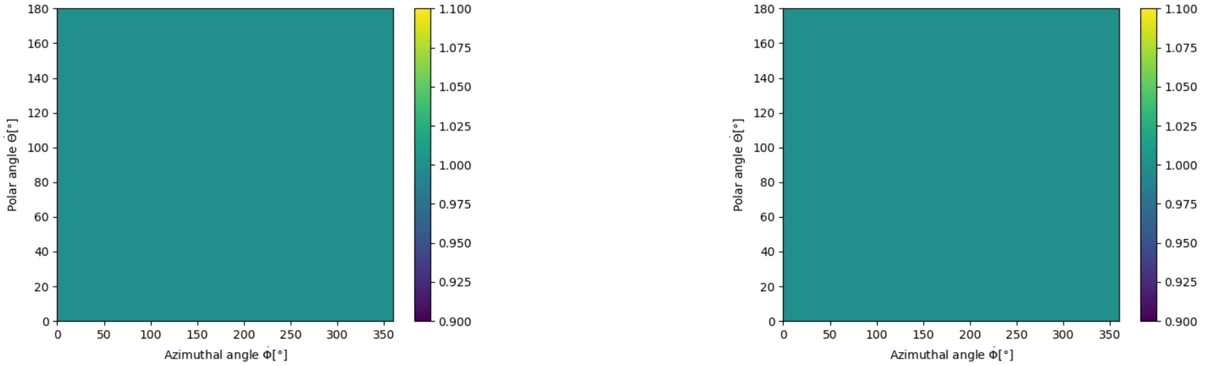

(c) The SkyMap of a 10 MeV proton with a radially inward trajectory resulted in 14400 (100%)hits from 14400 simulated trajectories.

(d) The SkyMap of a 10 MeV proton with a deviation of 5 ° resulted in 14400 (100%) hits from 14400 simulated trajectories.

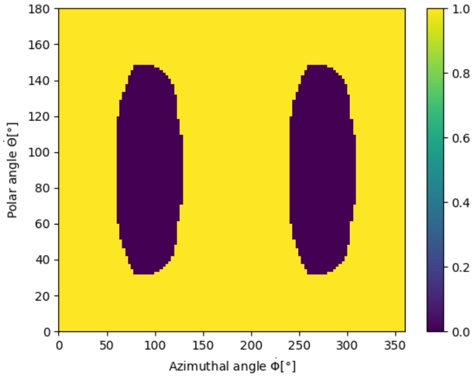

(e) The SkyMap of a 10 MeV proton with a deviation of 10 ° resulted in 11352 (78,8%) hits from 14400 simulated trajectories.

Figure 6.9: The five simulated SkyMaps show at which incident angles around the sphere the 10 MeV proton interacts with the detector indicated with the value "1" and the proton passes by the detector with the value "0".

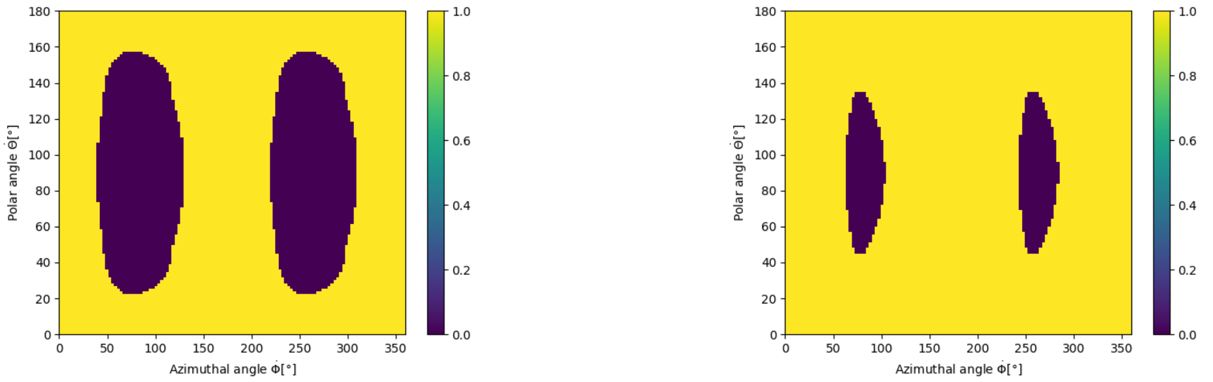

(a) The SkyMap of a 100 MeV proton with a deviation of -10 ° resulted in 9956 (69,1%) hits from 14400 simulated trajectories.

(b) The SkyMap of a 100 MeV proton with a deviation of -5 ° resulted in 13144 (91,3%) hits from 14400 simulated trajectories.

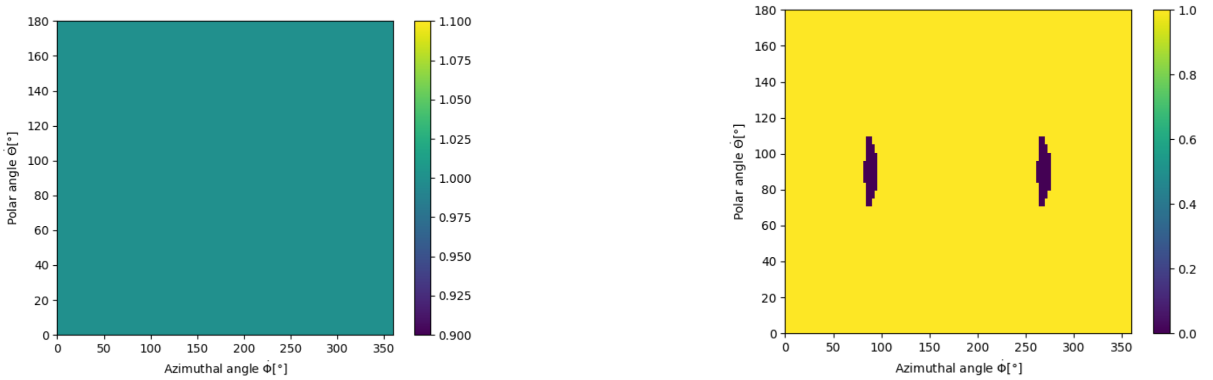

(c) The SkyMap of a 100 MeV proton with a radially inward trajectory resulted in 14400 (100%) hits from 14400 simulated trajectories.

(d) The SkyMap of a 100 MeV proton with a deviation of 5 ° resulted in 14212 (98,7%) hits from 14400 simulated trajectories.

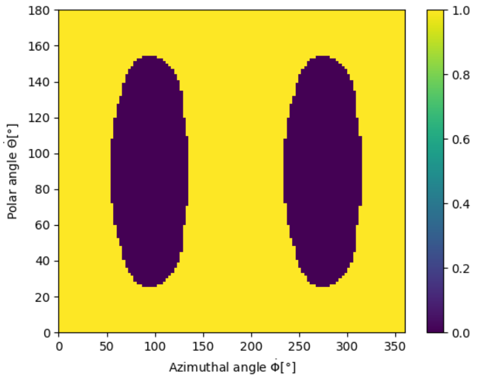

(e) The SkyMap of a 100 MeV proton with a deviation of 10 ° resulted in 10616 (73,7%) hits from 14400 trajectories.

Figure 6.10: The five simulated SkyMaps show at which incident angles around the sphere the 100 MeV proton interacts with the detector indicated with the value ”1” and the proton passes by the detector with the value ”0”.

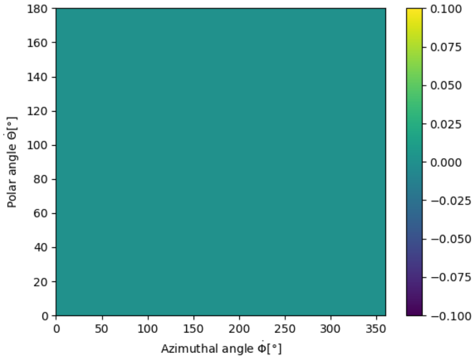

(a) The SkyMap of a 0.1 MeV electron with a deviation of -10 ° resulted in 0 hits from 14400 simulated trajectories.

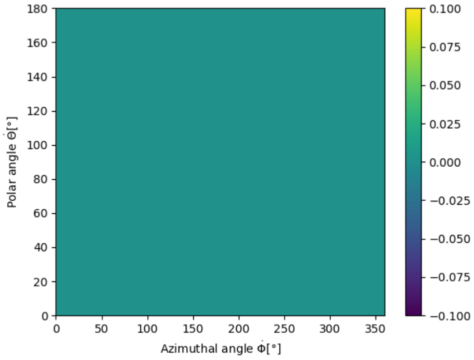

(b) The SkyMap of a 0.1 MeV electron with a deviation of -5 ° resulted in 0 hits from 14400 simulated trajectories.

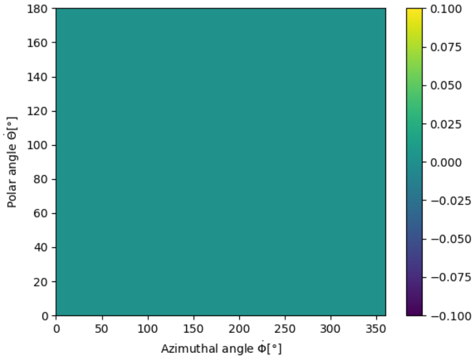

(c) The SkyMap of a 0.1 MeV electron with a radially inward trajectory resulted in 0 hits from 14400 simulated trajectories.

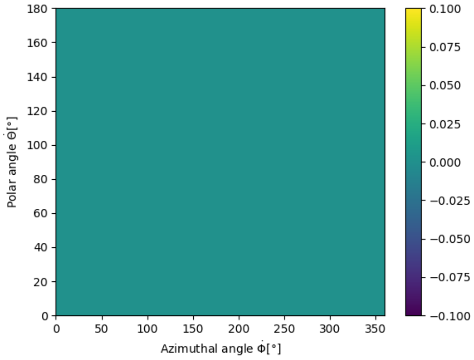

(d) The SkyMap of a 0.1 MeV electron with a deviation of 5 ° resulted in 0 hits from 14400 simulated trajectories.

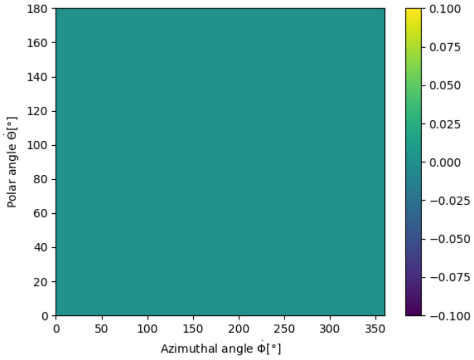

(e) The SkyMap of a 0.1 MeV electron with a deviation of 10 ° resulted in 0 hits from 14400 simulated trajectories.

Figure 6.11: The five simulated SkyMaps show at which incident angles around the sphere the 0.1 MeV electron interacts with the detector indicated with the value ”1” and the electron passes by the detector with the value ”0”.

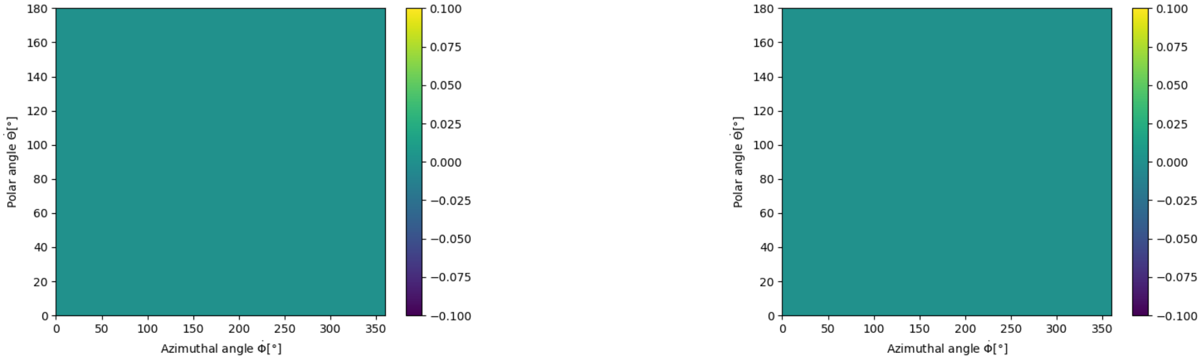

(a) The SkyMap of a 1 MeV electron with a deviation of -10 ° resulted in 0 hits from 14400 simulated trajectories.

(b) The SkyMap of a 1 MeV electron with a deviation of -5 ° resulted in 0 hits from 14400 simulated trajectories.

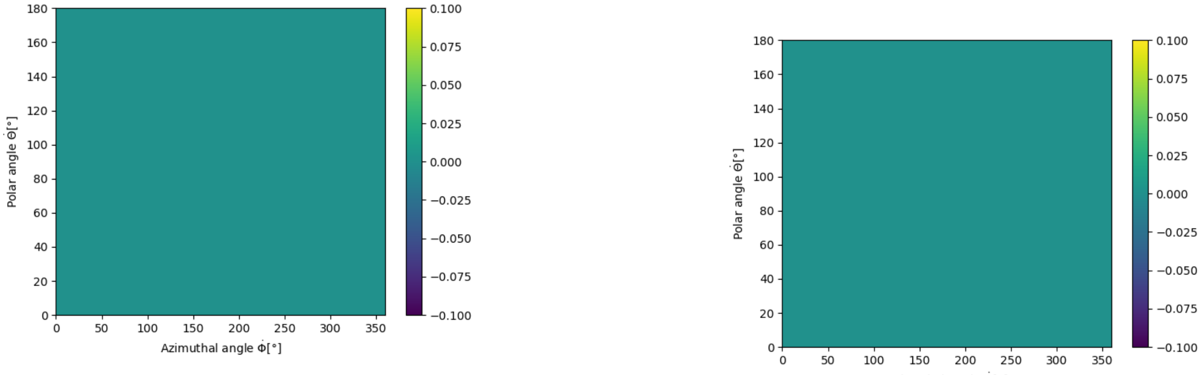

(c) The SkyMap of a 1 MeV electron with a radially inward trajectory resulted in 0 hits from 14400 simulated trajectories.

(d) The SkyMap of a 1 MeV electron with a deviation of 5 ° resulted in 0 hits from 14400 simulated trajectories.

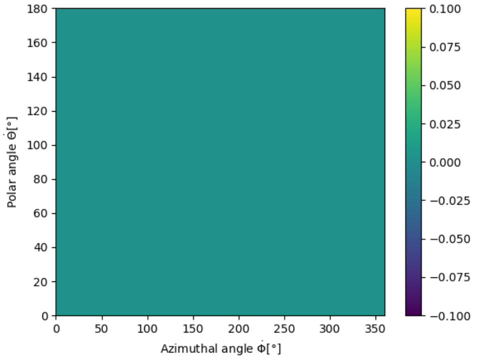

(e) The SkyMap of a 1 MeV electron with a deviation of 10 ° resulted in 0 hits from 14400 simulated trajectories.

Figure 6.12: The five simulated SkyMaps show at which incident angles around the sphere the 1 MeV electron interacts with the detector indicated with the value ”1” and the electron passes by the detector with the value ”0”.

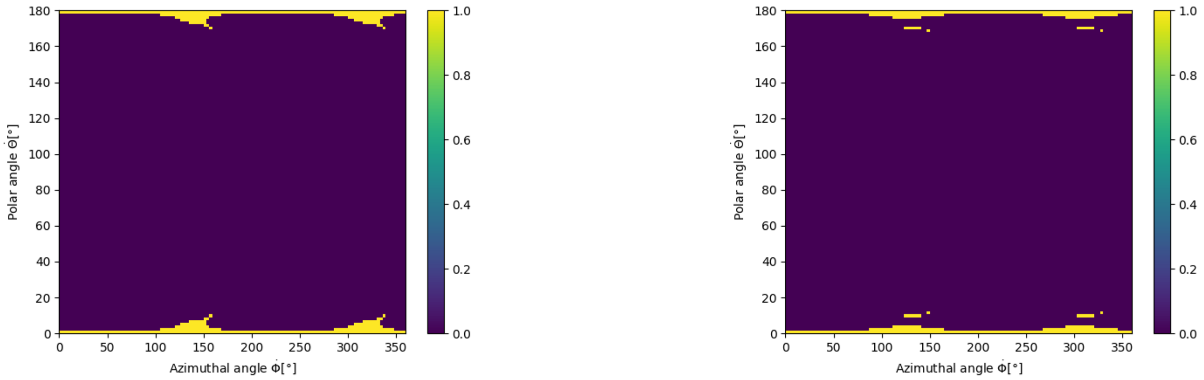

(a) The SkyMap of a 10 MeV electron with a deviation of -10 ° resulted in 444 (3,1%) hits from 14400 simulated trajectories.

(b) The SkyMap of a 10 MeV electron with a deviation of -5 ° resulted in 412 (2,9%) hits from 14400 simulated trajectories.

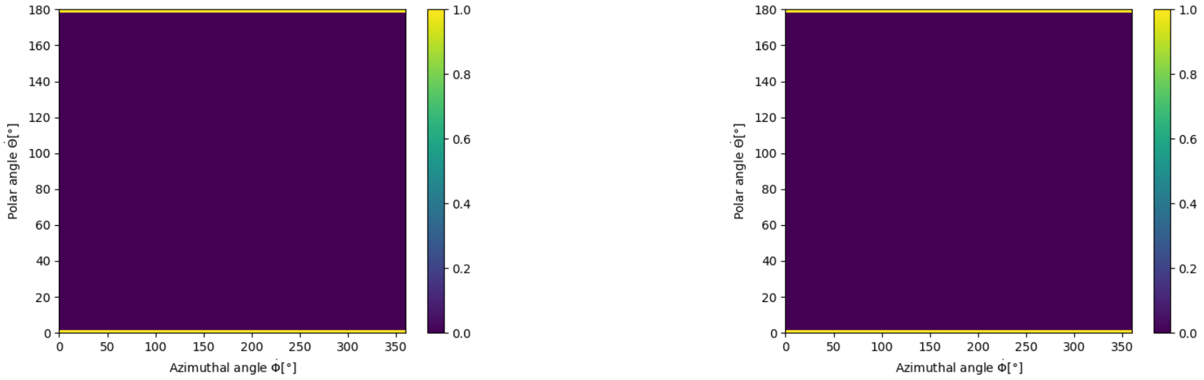

(c) The SkyMap of a 10 MeV electron with a radially inward trajectory resulted in 240 (1,7%) hits from 14400 simulated trajectories.

(d) The SkyMap of a 10 MeV electron with a deviation of 5 ° resulted in 240 (1,7%) hits from 14400 simulated trajectories.

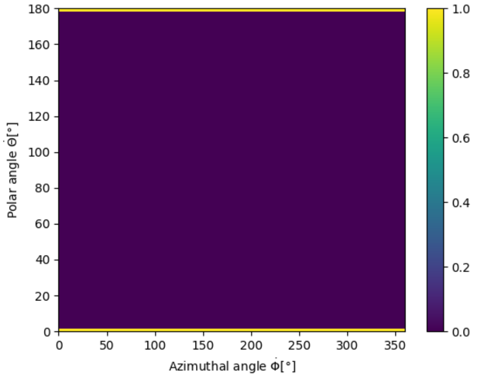

(e) The SkyMap of a 10 MeV electron with a deviation of 10 ° resulted in 240 (1,7%) hits from 14400 simulated trajectories.

Figure 6.13: The five simulated SkyMaps show at which incident angles around the sphere the 10 MeV electron interacts with the detector indicated with the value ”1” and the electron passes by the detector with the value ”0”.

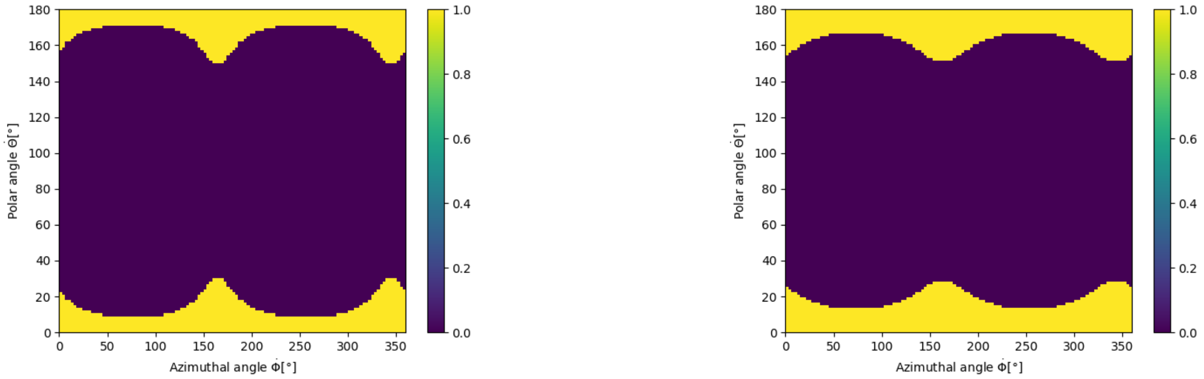

(a) The SkyMap of a 0.1 MeV helium nucleus with a deviation of -10 ° resulted in 2360 (16,4%) hits from 14400 simulated trajectories.

(b) The SkyMap of a 0.1 MeV helium nucleus with a deviation of -5 ° resulted in 3020 (21,0%) hits from 14400 simulated trajectories.

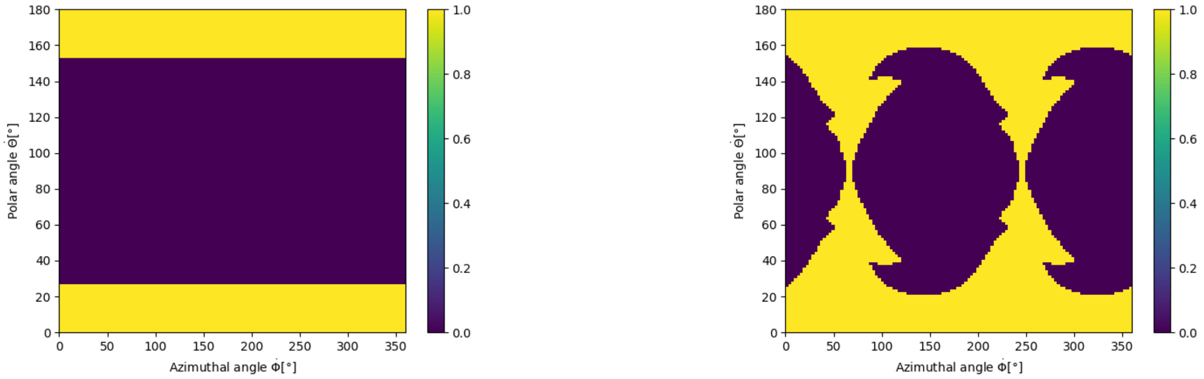

(c) The SkyMap of a 0.1 MeV helium nucleus with a radially inward trajectory resulted in 4320 (30,0%) hits from 14400 simulated trajectories.

(d) The SkyMap of a 0.1 MeV helium nucleus with a deviation of 5 ° resulted in 6760 (47,0%) hits from 14400 simulated trajectories.

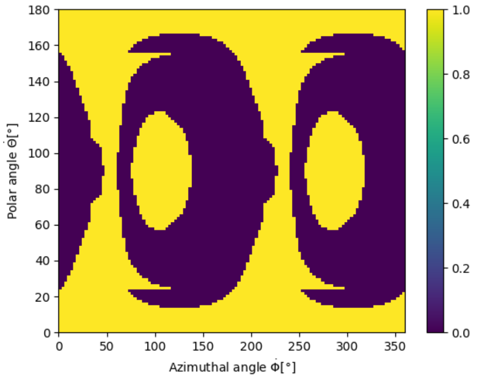

(e) The SkyMap of a 0.1 MeV helium nucleus with a deviation of 10 ° resulted in 6988 (48,5%) hits from 14400 simulated trajectories.

Figure 6.14: The five simulated SkyMaps show at which incident angles around the sphere the 0.1 MeV helium nucleus interacts with the detector indicated with the value ”1” and the helium nucleus passes by the detector with the value ”0”.

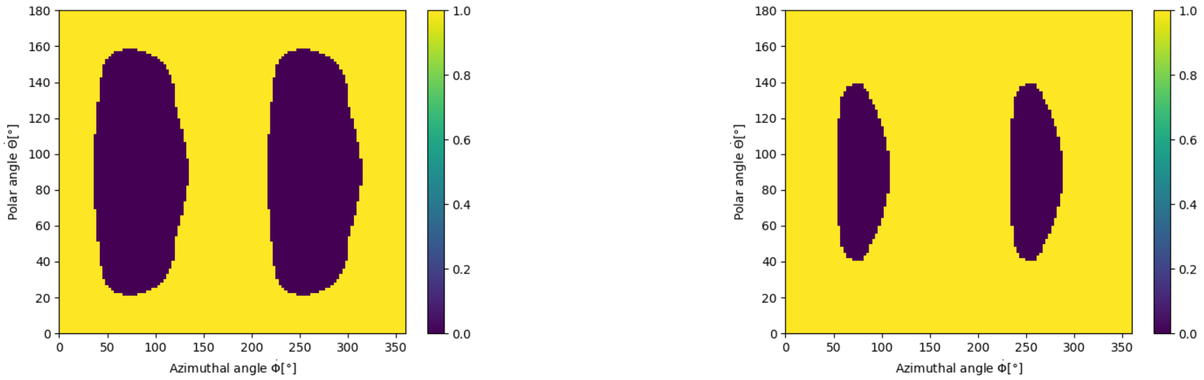

(a) The SkyMap of a 10 MeV helium nucleus with a deviation of -10 ° resulted in 9504 (66,0%) hits from 14400 simulated trajectories.

(b) The SkyMap of a 10 MeV helium nucleus with a deviation of -5 ° resulted in 12528 (87,0%) hits from 14400 simulated trajectories.

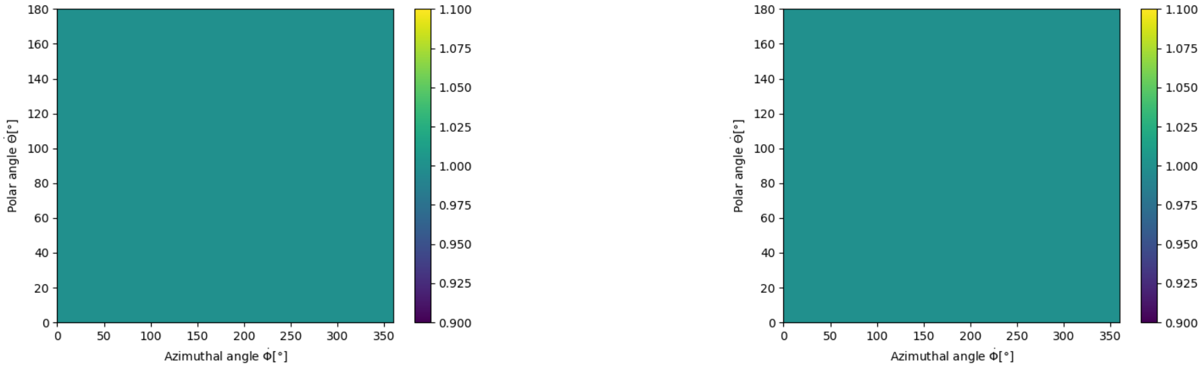

(c) The SkyMap of a 10 MeV helium nucleus with a radially inward trajectory resulted in 14400 (100%) hits from 14400 simulated trajectories.

(d) The SkyMap of a 10 MeV helium nucleus with a deviation of 5 ° resulted in 14400 (100%) hits from 14400 simulated trajectories.

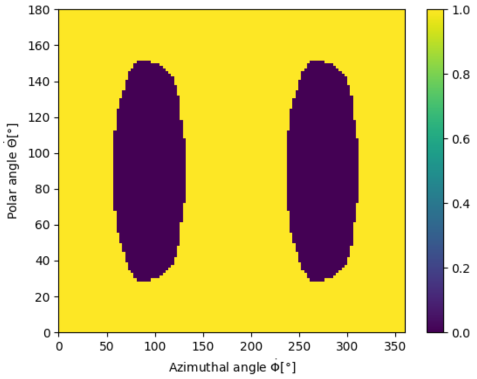

(e) The SkyMap of a 10 MeV helium nucleus with a deviation of 10 ° resulted in 11020 (76,5%) hits from 14400 simulated trajectories.

Figure 6.15: The five simulated SkyMaps show at which incident angles around the sphere the 10 MeV helium nucleus interacts with the detector indicated with the value ”1” and the helium nucleus passes by the detector with the value ”0”.

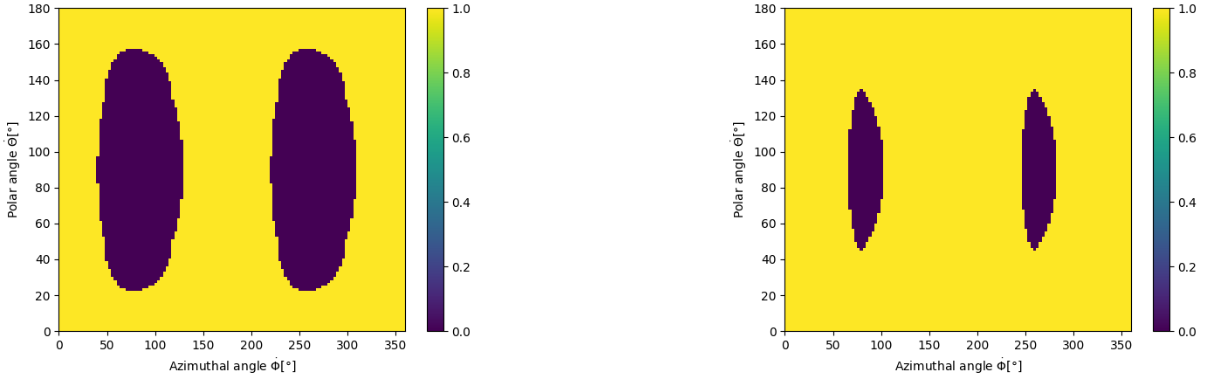

(a) The SkyMap of a 100 MeV helium nucleus with a deviation of -10 ° resulted in 10064 (69,9%) hits from 14400 simulated trajectories.

(b) The SkyMap of a 100 MeV helium nucleus with a deviation of -5 ° resulted in 13304 (92,4%) hits from 14400 simulated trajectories.

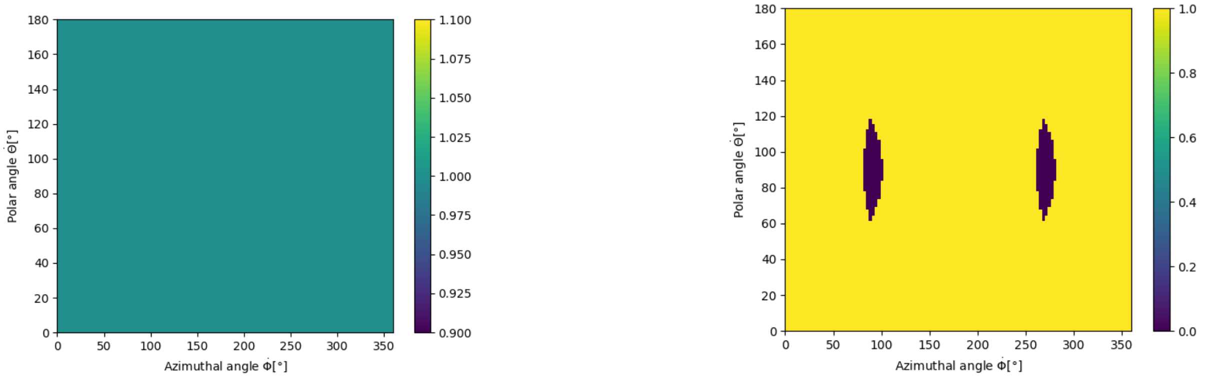

(c) The SkyMap of a 100 MeV helium nucleus with a radially inward trajectory resulted in 14400 (100%) hits from 14400 simulated trajectories.

(d) The SkyMap of a 100 MeV helium nucleus with a deviation of 5 ° resulted in 14048 (97,6%) hits from 14400 simulated trajectories.

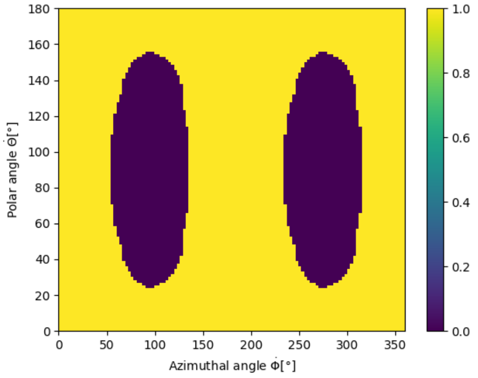

(e) The SkyMap of a 100 MeV helium nucleus with a deviation of 10 ° resulted in 10532 (73,1%) hits from 14400 simulated trajectories.

Figure 6.16: The five simulated SkyMaps show at which incident angles around the sphere the 100 MeV helium nucleus interacts with the detector indicated with the value ”1” and the helium nucleus passes by the detector with the value ”0”.

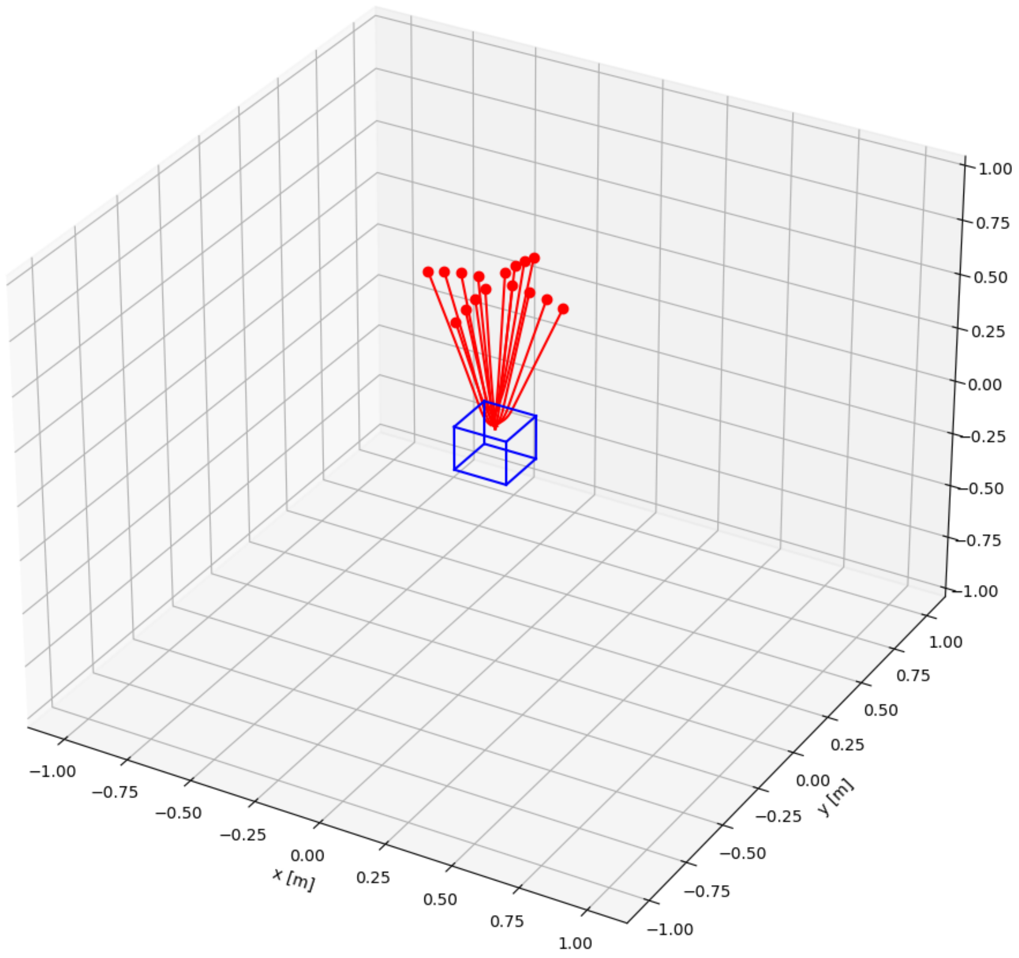

Figure 6.17: The 10 MeV electron and positron trajectories to visualize the collisions at the north pole of the cube-shaped detecting unit with the 10 T magnetic dipole field surrounding the detector.

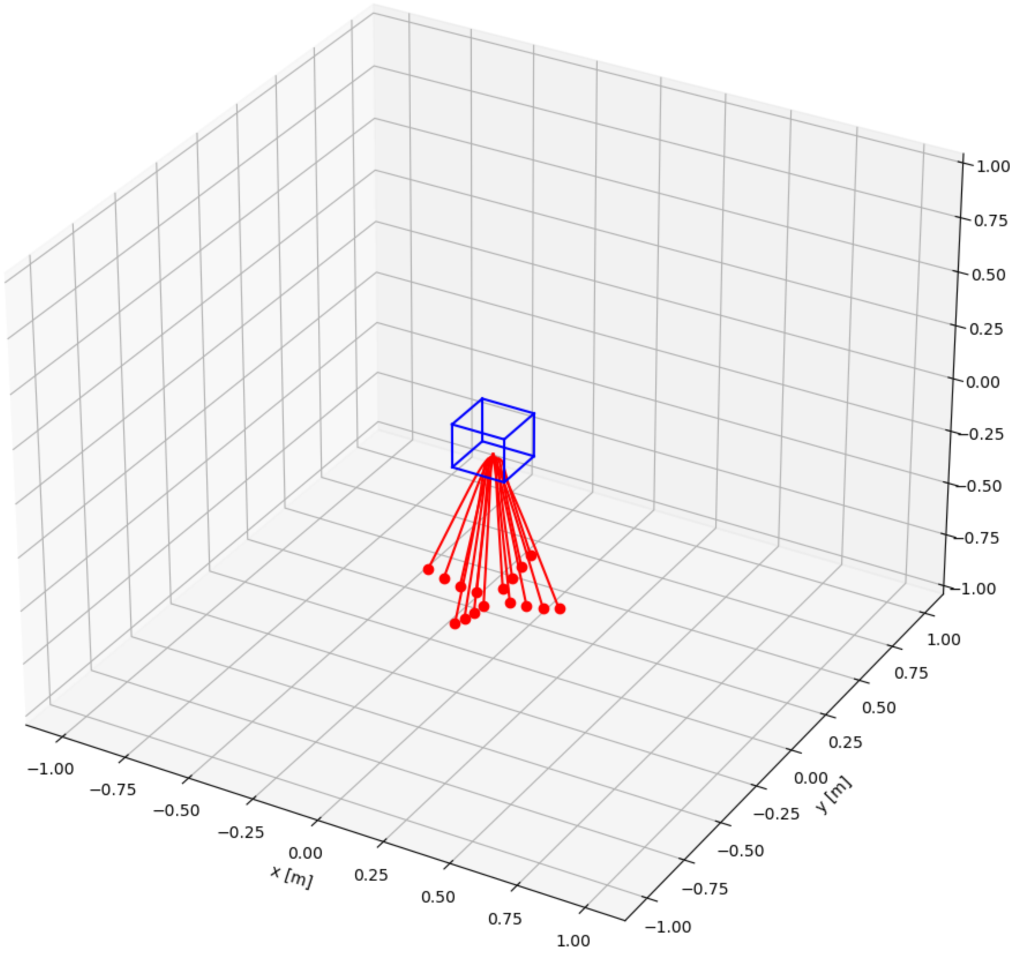

Figure 6.18: The 10 MeV electron and positron trajectories to visualize the collisions at the south pole of the cube-shaped detecting unit with the 10 T magnetic dipole field surrounding the detector.

Statutory declaration / Eidesstattliche Erklärung

I hereby declare that I have written the present thesis independently, that I have not used any other sources or aid than those indicated and that I have not yet or simultaneously submitted this thesis to any other examination board for the purpose of obtaining an academic degree.

Hiermit versichere ich, dass ich die vorliegende Arbeit in allen Teilen selbstständig angefertigt habe. Es wurden keine anderen Quellen und Hilfsmittel für indirekte und direkte Zitate, als die in der Arbeit aufgelisteten, verwendet. Alle Zitate sind kenntlich gemacht und nachvollziehbar ausgewiesen, dass diese geprüft werden können. Ebenso wurden Bildquellen durch die Angabe eines Links oder einer anderen Quelle kenntlich gemacht. Ich versichere, dass sämtliche bildnerische und gestalterische Werkstücke eigenständig angefertigt wurden. Die Arbeit wurde bisher oder gleichzeitig keiner anderen Prüfungsbehörde zur Erlangung eines akademischen Grades vorgelegt.

Altheim, 22.11.2023
Ort, Datum

Eric Nanowsky
Eric Nanowsky